Infrared and Fluorescent Thermal Imaging and Thermal Transport Characterization of Engineering Devices and Systems

by

SWAPNIL SURYAKANT SALVI

DISSERTATION

Submitted in partial fulfillment of the requirements

For the degree of Doctor of Philosophy at

The University of Texas at Arlington

August 2022

Arlington, Texas

Supervising Committee:

Dr. Ankur Jain (Committee Chairperson)

Dr. Ashfaq Adnan

Dr. Miguel Amaya

Dr. Hyejin Moon

Dr. Narges Shayesteh

Copyright by
Swapnil Suryakant Salvi
2022

ACKNOWLEDGEMENTS

I would like to express my sincere gratitude and appreciation to my supervisor, Professor Ankur Jain for believing in me and giving me the opportunity to start my research in his lab – Microscale Thermophysics Laboratory – where I have developed a keen interest in heat transfer and energy storage and conversion systems. He was always supportive, inspiring, and passionate about research. He certainly made me a better researcher and successfully played a true role as our academic father. I am sure there won't be a single problem I will solve in my career without thinking of the ways he taught us to tackle them.

I would really like to thank my dissertation committee for their time, guidance, and support. Their valuable suggestions helped me to improve the quality of my dissertation.

I would like to thank my family who provided me invaluable emotional and financial support throughout this journey. I would like to thank them for understanding my ambition for this degree. Without their support, my success would have not been possible. I am forever grateful to have an understanding, supportive and encouraging family. I would like to thank my friends – my family in US – Vrushali, Hardik, Rajat and Mohana for being there whenever I needed them mentally or emotionally.

I would like to thank my lab seniors who helped me grow – Dr. Hardikkumar Prajapati, Dr. Mohammad Parhizi, Dr. Amirhossein Mostafavi, Dr. Darshan Ravoori and Dr. Momen Qasaimeh. I would also like to thank everyone at Microscale Thermophysics Laboratory for providing productive suggestions and helping me at various stages of research.

Special thanks to MAE department at the University of Texas at Arlington for all their support. I would also like to thank National Science Foundation for their financial support for my research and Summer internship. Without their support, this journey could not have accomplished.

I would like to sincerely thank Dr. Bapiraju Surampudi and Ian Smith for their invaluable help and support in my NSF internship grant application. I would also like to thank both of them for being a great mentor during my internship. I would like to thank Dr. Andre Swarts, Christopher Kelly and Matthew Kubesh for their help and support during my internship.

August 12, 2022.

ABSTRACT

Infrared and Fluorescent Thermal Imaging and Thermal Transport Characterization of Engineering Devices and Systems

Swapnil Suryakant Salvi, Ph.D.

The University of Texas at Arlington, 2022

Supervising Professor: Dr. Ankur Jain

Infrared (IR) thermal imaging is widely used for non-contact temperature measurement in engineering. IR camera detects thermal emissions from the target surface in a certain wavelength range, which, using the known surface emissivity, can be converted to a pixel-by-pixel temperature map. Fluorescence imaging also works along similar lines.

This Ph.D. dissertation contributes towards thermal imaging and thermal transport characterization in engineering devices/systems using infrared and fluorescence imaging. In the first two parts of this work, infrared thermal imaging is used for measuring thermal conductivity of thin wires and for spotting unusual activities in a three-dimensional integrated circuit (3D IC). In the third part, a fluorescence imaging technique is developed for non-contact temperature measurement of a Li-ion cell with the help of a standard camera (mobile or DSLR).

Measuring and understanding thermal conductivity is key for thermal characterization of materials and for maximizing performance and thermal safety of engineering devices and systems. This study presents a comparative method for measuring thermal conductivity of a thin wire. The method is based on infrared thermography of the wire of interest suspended from a high temperature base. Through comparison of thermal response of the wire with that of a standard wire of known properties, thermal conductivity is measured for several wires in a broad range of thermal

conductivity. Measurements are reported for both low thermal conductivity polymer wires and high thermal conductivity metal wires.

In the second part, infrared thermal imaging along with image analysis algorithms have been used for hardware trojan detection in microprocessors. Modern microprocessors are highly susceptible to hardware and software Trojans. Such Trojan activities may slow down the microprocessor, or in a worse case, leak confidential data and incapacitate microprocessor functionality. In principle, abnormal circuit activity due to Trojan operation is expected to cause distortion in the temperature field of the IC due to Joule heating. This study carries out measurement of temperature field of the transistor plane of a two-die three-dimensional integrated circuit (3D IC) thermal test chip through backside infrared imaging. Four distinct image processing algorithms are evaluated and compared in terms of speed, accuracy and occurrence of false positives and negatives.

Finally in the third part, analysis for accelerated aging has been carried out for a 21700-battery module using immersed cooling for heat dissipation. Results with immersed cooling are compared with the baseline case of cooling with just stagnant air. Multiple hypotheses are checked in order to find the reasons behind deteriorated performance in terms of life of the battery. These hypotheses are analyzed using theoretical modeling as well as experimental measurements. Electrochemical impedance spectroscopy (EIS) is carried out to check the possibility of lithium plating, one of the possible reasons for accelerated aging of specified batteries.

Table of Contents

ACKNOWLEDGEMENTS III
ABSTRACT V
Chapter 1 1
1-1. Introduction 1
Chapter 2 Measurement of thermal conductivity of millimeter-sized wires using the fin effect ... 4
2-1. Introduction 5
2-2. Theoretical Treatment 8
2-3. Experiments 11
2.3.1. Experimental setup 11
2.3.2. Experimental procedure 13
2.3.3. Reference thermal conductivity measurements 14
2-4. Results and discussion 16
2.4.1. Temperature data and comparative determination of k_T 16
2.4.2. Measurements on wires of different diameters 20
2.4.3. Impact of experimental conditions on measurement accuracy 22
2.4.4. Measurement of thermal conductivity of solder wires 24
2.4.5. Validity of infinite fin assumption 25
2.4.6. Uncertainty analysis 26
2-5. Nomenclature 27
Chapter 3 Detection of Unusual Thermal Activities in a Semiconductor Chip using Backside Infrared Thermal Imaging 28
3-1. Introduction 29
3-2. Experimental Setup 32
3-3. Image Processing Techniques 34
3.3.1. Binary comparison method 35
3.3.2. Structural similarity (SSIM) index method [71] 35
3.3.3. 2-D correlation coefficient method [74] 36
3.3.4. Histogram comparison method [76] 36
3-4. Results and Discussion 37
3.4.1. Temperature colormaps 37
3.4.2. Algorithm-based detection with top die resistor activated 39
3.4.3. Algorithm-based detection of heating pulse with background thermal activity 42
3.4.4. Validity of backside infrared imaging 45

Chapter 4 Experimental and Theoretical Analysis of Immersion Cooling of a 21700 Li-Ion Battery Module and its Impact on Accelerated Cell Aging 47
4-1. Introduction 48
4-2. Experimental apparatus 50
4.2.1 Experimental setup 51
4.2.2 Experimental procedure 55
4-3. Theoretical modeling 57
4.3.1 Analytical modeling 57
4.3.2 Simulink modeling 60
4.3.3 Numerical modeling 60
4-4. Results and Discussion 61
4.4.1 Hypotheses for Capacity Fade 61
4.4.2 Baseline Case Results Discussion 63
4.4.3 Fluid-X Immersion Cooled Case Results Discussion 64
4.4.4 Cell Core Temperature Measurement Discussion 66
4.4.5 EIS Results and Lithium Plating Discussion 68
4-5. Nomenclature 69
REFERENCES 70
Chapter 5 Conclusion 79
5-1. Conclusion 79
BIOGRAPHICAL INFORMATION 82

Chapter 1

1-1. Introduction

Infrared (IR) thermal imaging is widely used for temperature measurement in the engineering fields. IR camera detects the thermal emissions from the target surface, converts it into an electronic signal, which further will be processed to produce an image consisting of individual temperature values for each pixel. Though the emissivity of target surface must be known for accurate measurements. In the first two projects, the use of infrared thermal imaging is done for measuring thermal conductivity of thin wires and for spotting unusual activities in a three-dimensional integrated circuit (3D IC). In the third and ongoing project, fluorescence is used to measure the temperature of a li-ion cell with the help of a standard camera (mobile or DSLR). In both the thermal imaging techniques there are multiple benefits like non-contact and non-destructive nature of measurements. Another recently completed project is an industrial collaborative research work, focused on the effects of li-ion battery operational parameters on cell aging and performance.

Measuring and understanding thermal conductivity is key for thermal characterization of materials and for maximizing performance and thermal safety of engineering devices and systems. Samples around a few mm size are typically too large for microscale methods but may be too small for the standard macroscale methods. Measurement of thermal conductivity of thin wires is critical for multiple engineering applications that involve heat transfer in thin wires. This study presents a comparative method for measuring thermal conductivity of a thin wire. The method is based on infrared thermography of the wire of interest suspended from a high temperature base. Through comparison of thermal response of the wire with that of a standard wire of known properties,

thermal conductivity is measured for several wires in a broad range of thermal conductivity. Measurements are reported for both low thermal conductivity polymer wires and high thermal conductivity metal wires. Results are found to be in good agreement with expected values of thermal conductivity. Results presented in this work contribute towards addressing an important thermal metrology need and may help improve thermal design of a broad range of engineering applications that utilize thin wires.

In the next project, infrared thermal imaging along with image analysis algorithms have been used for a hardware trojan detection in microprocessors. Modern microprocessors are highly susceptible to hardware and software Trojans. Such Trojan activities may slow down the microprocessor, or in a worse case, leak confidential data and incapacitate microprocessor functionality. As a result, the detection and disablement of Trojans – both hardware and software – is recognized to be a critical security need for semiconductor chips, particularly for sensitive applications, such as defense, banking, etc. In principle, abnormal circuit activity due to Trojan operation is expected to cause distortion in the temperature field of the IC due to Joule heating. This study carries out measurement of temperature field of the transistor plane of a semiconductor device through backside infrared imaging. Chip temperature is one such parameter that is closely related to the degree of Trojan activity. This paper carries out backside infrared imaging of a two-die three-dimensional integrated circuit (3D IC) thermal test chip to detect unusual thermal activities on the chip. Four distinct image processing algorithms are evaluated and compared in terms of speed, accuracy and occurrence of false positives and negatives. This work may help develop thermal imaging as a means for real-time Trojan detection and enhancement of security of modern semiconductor chips, including 3D IC.

Additionally, one of the recently completed projects focuses on the effects of immersed cooling for a 21700 li-ion battery module on accelerated cell aging observed experimentally. Overheating of Li-ion cells and battery packs is an ongoing technological challenge for electrochemical energy conversion and storage in multiple engineering systems, including electric vehicles. Immersion cooling is a promising thermal management technique to address these challenges. This work presents experimental and theoretical analysis of thermal and electrochemical impact of immersion cooling of a small module of Li-ion cells. Measurements of surface and core temperature rise in the presence of immersion cooling are reported. Significant reduction in temperature rise compared to the baseline case is observed. However, immersion cooling is also found to result in a small but non-negligible increase in capacity fade of the cells. A number of hypotheses are formed and systematically tested through comparison of experimental measurements with theoretical modeling and simulations. It is found that the theoretical models developed for predicting the surface as well as core temperatures for a li-ion module under immersion cooling matches well with the experimental results. Whereas EIS measurement confirms the cell ageing and SEI growth, it also enlightens the likelihood of lithium plating which increases the probability of being an indirect reason for ageing. The results presented in this work quantify both thermal and electrochemical impact of an important thermal management technique for Li-ion cells. These results may find direct application in the design and optimization of electrochemical energy conversion and storage systems.

Chapter 2

Measurement of thermal conductivity of millimeter-sized wires using the fin effect

Published as: Salvi, S. S., Jain, A., "Measurement of thermal conductivity of millimeter-sized wires using the fin effect", *Applied Thermal Engineering*, **178**, pp. 115482:1-9, 2020.

2-1. Introduction

Measuring and understanding the nature of thermal conductivity is important for thermal characterization of materials and for maximizing performance and thermal safety of a variety of engineering devices and systems. As defined by Fourier law, thermal conductivity is a key thermophysical property that relates heat flux with temperature rise. While in general, thermal conductivity is anisotropic and a function of temperature, it is often treated, within engineering approximation to be isotropic and independent of temperature.

A number of experimental techniques exist for measurement of thermal conductivity. In general, these methods rely on measurement of the thermal response of the sample of interest to an imposed heat flux or temperature gradient [1–3]. The experimentally measured thermal response is usually compared with an analytical heat transfer model to determine thermal conductivity. For example, in a commonly used measurement method [2], the material of interest is sandwiched between two plates maintained at two different temperatures, and the measured heat flux is compared with the Fourier law to determine thermal conductivity. Measurements are often carried out on two samples of different thicknesses to account for sample-to-instrument thermal contact resistance [4]. A sample of well-known thermal conductivity is also often inserted in series in order to accurately measure heat flux. A guard heater [5] is often used to minimize stray heat losses. Transient measurements [1,6] are also often used to measure thermal conductivity. For example, the transient plane source method [3] utilizes a thin film metal heater/sensor sandwiched between two large, identical samples. The measured temperature as a function of time is compared with an analytical model for heat transfer into infinite media to determine thermal conductivity. In the laser flash method [7], an energy pulse is deposited on one face of a sample and temperature rise on the other face is measured using an infrared sensor. Comparison with a well-known

analytical model results in determination of thermal diffusivity. Comparison of thermal response of the sample with that of a material of well-known properties is used to determine heat capacity, so that thermal conductivity can then be calculated. Each of these methods offers certain advantages and disadvantages. For example, the laser flash method is non-contact and does not involve thermal contact resistance [8]. However, this method requires extensive sample preparation. On the other hand, the transient plane source requires samples of a certain minimum size depending on the expected thermal diffusivity and measurement capability [9,10].

In addition to the macroscale thermal property measurement techniques summarized above, a number of techniques developed specifically for microscale material samples are also available. In general, most of these methods may be classified into electrical-based [11,12] and optical-based methods [13–15]. In the first category, Joule heating in the form of direct [12,16] or alternating current [11,17] is imposed and the ensuing thermal response is used to determine thermal conductivity. The three-omega method [18] is an example, which has been extensively used for a variety of applications [18]. In optical methods, heating is provided using an optical signal, and temperature is also usually measured optically in a pump-and-probe configuration. Thermoreflectance based methods [19–21] are another good example of optical-based methods. Such methods have been extensively used for characterization of thermal properties of micro- and nano-scale materials [22], as well as for more macroscale materials [23,24].

Unfortunately, most measurement techniques outlined above are not appropriate for thin wires. For example, while imposing and measuring a steady-state heat flux through a flat sample of large cross-section is easily implemented in measurement methods, doing so on a wire is challenging due to difficulties in precisely measuring heat flux through the thin wire, as well as

heat loss from the wire perimeter. Several engineering applications such as electrical wires, filaments for additive manufacturing, solder wires, welding electrodes, etc. involve heat transfer in wires, and therefore, understanding thermal conductivity of wires for these applications is critical. For example, in polymer-based additive manufacturing, understanding thermal conduction in the filament is critical for ensuring good filament-to-filament adhesion [25,26]. As another example, the reliability and lifetime of a non-consumable welding electrode depends critically on its heat dissipation capabilities in the controlled atmosphere [27,28]. Finally, heat transfer in solder wires is also important for ensuring good process quality [29,30], and therefore, understanding thermal conductivity of the solder wires is important. While the thermal conductivity of molten solder material has been reported [31], similar data are not available for solid solder wire.

Despite the importance of understanding and characterizing heat transfer in applications discussed above, there is a lack of systematic measurement methods for thin wires. A recent paper presented a fin-based method to compare thermal conduction in two strands of hair and correlate with moisture content and hair type [32]. However, this work did not report absolute values of the thermal conductivities of the hair being investigated.

This project presents an experimental technique to measure the thermal conductivity of thin wires using infrared thermography-based measurement of temperature distribution along the wires when suspended from a high temperature block. The method is based on comparison of thermal response of the test wire with that of a standard wire of known thermal conductivity in the same surrounding environment. Wires of materials of a broad range of thermal conductivity are characterized. Good accuracy is reported for both low and high thermal conductivity wires. As an application of this measurement technique, thermal conductivity values of different solders are

measured and reported. The fundamental theory behind this method utilizes the fin effect, which is quite standard, however, measurement of thermal conductivity of wires based on this approach has not been reported in the past.

Theoretical modeling of the measurement method is discussed in section 2. Experimental setup and experimental procedure is presented in Section 3. Results are presented and discussed in section 4.

2-2. Theoretical Treatment

Consider a long cylindrical wire of length l and diameter D, for which, measurement of axial thermal conductivity k is of interest. k is assumed to be constant and isotropic. As shown in Figure 1(b), consider the wire to be attached at one end to a large body maintained at a constant temperature T_b. The wire loses heat from its periphery to the ambient temperature T_a due to convection. The wire is assumed to be long enough, so that the infinite fin assumption is appropriate for analytical modeling. The validity of this assumption for the wires used in this work is discussed in Section 4.5. Aspect ratio of the wire is assumed to be very large, so that thermal conduction in the wire is one-dimensional. Further, the radial Biot number is calculated to be 0.04 or less for the experimental conditions, due to which, thermal gradient in the radial direction is expected to be negligible. Temperature rise during the experiment is assumed to be small enough, such that radiative heat transfer can be modeled using a linearized radiative heat transfer coefficient. Under these conditions, steady state temperature distribution in the wire is governed by the well-known fin equation [33]

$$\frac{d^2\theta}{dx^2} - \frac{hP}{kA_C}\theta = 0 \quad (1)$$

Where, $\theta = T(x) - T_a$ is the temperature rise above ambient. Further, $P = \pi D$ and $A_C = \frac{\pi D^2}{4}$ are the perimeter and cross-section area, respectively. h is the effective heat transfer coefficient that accounts for both convection and radiation and is assumed to be independent of temperature. Boundary conditions associated with equation (1) are

$$\theta(x = 0) = \theta_b \quad (2)$$

$$\theta \rightarrow 0 \;\; as \;\; x \rightarrow \infty \quad (3)$$

Temperature distribution in the fin can be easily derived to be [33]

$$\frac{\theta}{\theta_b} = e^{-mx} \quad (4)$$

where $m^2 = \frac{hP}{kA_c}$.

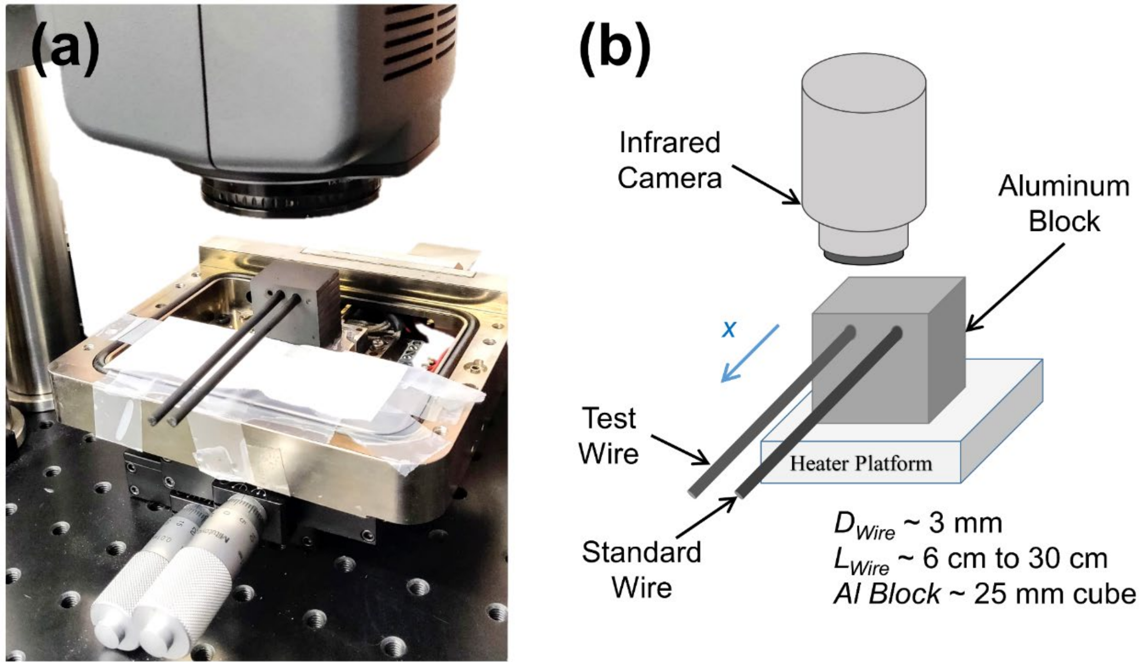

Figure 1: (a) Picture of the experimental setup showing the infrared camera, graphite-coated standard and test wires and a hot Aluminum block, (b) Schematic of the experimental setup.

Equation (4) shows that the parameter m can be determined from the slope of the plot of $\log(\theta/\theta_b)$ versus x. Further, provided the wire geometry and convective heat transfer coefficient h are known, the unknown thermal conductivity of the wire can be determined. However, while the wire geometry is usually known in advance, convective heat transfer around the wire is, in general, very difficult to measure, and therefore, a definitive value of h is not known.

In order to determine thermal conductivity without explicitly knowing the convective heat transfer coefficient, a comparative analysis is considered, wherein two wires – a test wire T of unknown thermal conductivity k_T and standard wire S of known thermal conductivity k_S – are considered. Both wires are subjected to the same ambient conditions, such as shown in Figures 1(a) and 1(b), so that the ratio of the slopes of $\log(\theta/\theta_b)$ versus x plots for the two wires is given by

$$\frac{m_S}{m_T} = \sqrt{\frac{k_T D_T}{k_S D_S}} \tag{5}$$

Equation (5) assumes the same convective heat transfer coefficient for both wires, which is reasonable if the two wires are of similar diameter and are measured simultaneously in the same ambient conditions. Equation (5) can be simplified to

$$k_T = k_S \frac{m_S^2 D_S}{m_T^2 D_T} \tag{6}$$

Equation (6) shows that the unknown thermal conductivity of the test wire, k_T, can be determined from the known thermal conductivity of the standard wire, k_S, based on the ratio of wire diameters, as well as the ratios of the m^2 values determined from experimental measurement of temperature distributions along the wires. Such a measurement will require a method such as infrared thermography to determine the entire temperature distribution along the wire in a non-

contact manner. Note that while equation (6) indicates that the test and standard wires may be chosen to have different diameters, significantly different diameters may result in different convective heat transfer coefficient, since convective heat transfer from a heated wire in general depends on the wire diameter [33–35] in both forced and natural convection conditions.

Even though the theory outlined above is based on the well-known fin effect [34], the authors are unaware of the use of these results for measurement of thermal conductivity of wires, as described above.

The next section discusses experimental design and setup for thermal conductivity measurement.

2-3. Experiments

Based on the theoretical method described in Section 2, experiments are carried out to measure the thermal conductivity of thin wires in a broad range of thermal conductivity values.

2.3.1. Experimental setup

As shown in Figure 1(a), the test wire with unknown thermal conductivity and a standard wire with known thermal conductivity are both suspended from a 25 mm by 25 mm by 25 mm Aluminum block using a metallic wire holding fixture that is designed to position the wires horizontally. The two wires are mounted close to each other, so that both experience the same ambient conditions, but not too close so that there is no thermal cross-talk. Through trial experiments, it is found that a wire-to-wire gap of 3.0 mm results in no thermal interactions between the two wires, whereas lower gaps are found to result in undesirable heat transfer between wires. Therefore, all experiments in this project are carried out with a wire-to-wire gap of 3.0 mm.

The theoretical model in section 2 assumes that radiation can be accounted for with a linear radiative heat transfer coefficient, and that temperature-dependence of the convective heat transfer coefficient is negligible. The temperature rise in experiments is limited to 20 °C in order to ensure that the validity of these assumptions.

The positioning of wires relative to the infrared camera lens can be altered using a dial operated sliding table arrangement. The Aluminum block is placed on an Instec HCS662V thermal stage that can be maintained at a constant temperature. Thermal interface material is applied between the Aluminum block and Instec stage, as well as between the block and wires to minimize interfacial temperature drop. Temperature distribution along the wires is measured using an FLIR A6703sc InSb infrared camera with a spatial resolution of around 15 μm and Noise Equivalent Temperature Difference of around 20 mK. Both wires are thermally imaged simultaneously. In each case, the wire length is chosen in order to satisfy the long wire assumption of the theoretical model. Depending on the wire length, this may result in measurement of only a portion of the long wire at a time instead of the entire wire. Additional length of the wire can be measured by moving the positioning stage that results in linear shift of the wire with respect to the infrared camera. Both wires are coated with a thin graphite spray in order to ensure uniform surface emissivity. Since the graphite spray is only a very thin film, it is not expected to significantly change thermal properties of the wire. Similar to past experiments [36,37], calibration of the infrared camera is carried out in advance. Infrared emission from a surface coated with the graphite spray is measured at a number of known temperatures, and the emissivity is chosen to be the value that results in closest agreement between the known temperatures and those determined from the measured infrared emission.

Figure 1(a) presents a picture of the experimental setup. Figure 1(b) depicts a schematic of the experimental setup, including dimensions and coordinate systems for the theoretical model.

2.3.2. Experimental procedure

Several experiments are carried out on high k metal and low k polymer wires using suitable standard wires of known thermal conductivity. In each case, the wires are chosen to be around 60 mm and 300 mm long for polymers and metals, respectively. Infrared thermography of the entire wire is carried out to ensure that the infinite fin assumption is valid. This is discussed in more detail in Section 4.5. Since temperature distribution in the wire decays exponentially, temperature rise in the wire closer to the tip can be small and noisy, which can distort the thermal conductivity measurement. Accordingly, temperature measurement close to the tip is not considered for determining thermal conductivity. The length of the wire to be considered for thermal conductivity measurements is determined by plotting $\log(\theta/\theta_b)$ as a function of x and determining the length beyond which the plot is not linear due to low and noisy temperature measurement.

In each experiment, the standard wire is chosen to be such that the test and standard thermal conductivities are in the same order of magnitude. This ensures that the slopes of temperature distributions are close to each other and eliminates error inherent in measuring relatively large or small slopes.

In each experiment, the Instec heating stage temperature is set to a specific value and allowed to reach steady state. The set temperature is chosen to be 35 ºC and 45 ºC for polymer and metal wires, respectively. The higher temperature for metallic wires is needed for reasonable signal-to-noise ratio, given the relatively high thermal conductivity of metals. Once thermal steady state is reached, temperature distribution along each wire is measured using the infrared camera.

Both wires are designed to be long enough so that temperature at the tip of the wires is close to ambient temperature. Forced air flow from an external fan is utilized in some experiments, particularly for metal wires, in which case the increased convective heat transfer coefficient due to forced air flow helps achieve the long fin assumption.

2.3.3. Reference thermal conductivity measurements

Two independent thermal conductivity measurement techniques are used for determining thermal conductivity of standard samples and validation of thermal conductivity measured using the proposed method. The laser flash method involves deposition of a pulse of energy on one face of a thin cylindrical sample while temperature rise on the other face is measured using an infrared detector. An analytical model for heat transfer in the sample [7] shows that temperature rise on the back side of the sample is given by

$$T(t) = T_{max} \cdot \left[1 + 2\sum_{n=1}^{\infty}(-1)^n \exp\left(-\frac{n^2\pi^2\alpha t}{L^2}\right)\right] \tag{7}$$

Where L and α are the sample thickness and thermal diffusivity, respectively. Comparison of experimental data with equation (7) results in determination of thermal diffusivity of the sample. Corrections to account for finite width of the heating pulse are taken into account. Further, comparative measurement of the peak temperature rise between the sample and a standard material is used to determine heat capacity. These measurements together help determine thermal conductivity of the sample. These measurements are carried out on a Netzsch LFA467 instrument. Since this method requires samples of relatively large diameter, the measurements are carried out on samples made of the same material as the wires of interest. Both wires are purchased from the

same manufacturer. This ensures that thermal conductivity of the sample being tested is the same as that of the wire of interest.

A one-dimensional, steady state heat flux method is also used in some cases to independently determine thermal conductivity of the wire materials being investigated in this work. This method, implemented in a TA Instruments Fox50 instrument, sandwiches a thin sample of the material of interest between two plates maintained at different temperatures. Measurement of the resulting heat flux through the material at steady state helps determine total thermal resistance. The effect of thermal contact resistances between the material and hot/cold plates is accounted for by two independent measurements of samples of different thicknesses. Similar to the laser flash method, these measurements are carried out on larger samples made of the material of interest purchased from the same manufacturer.

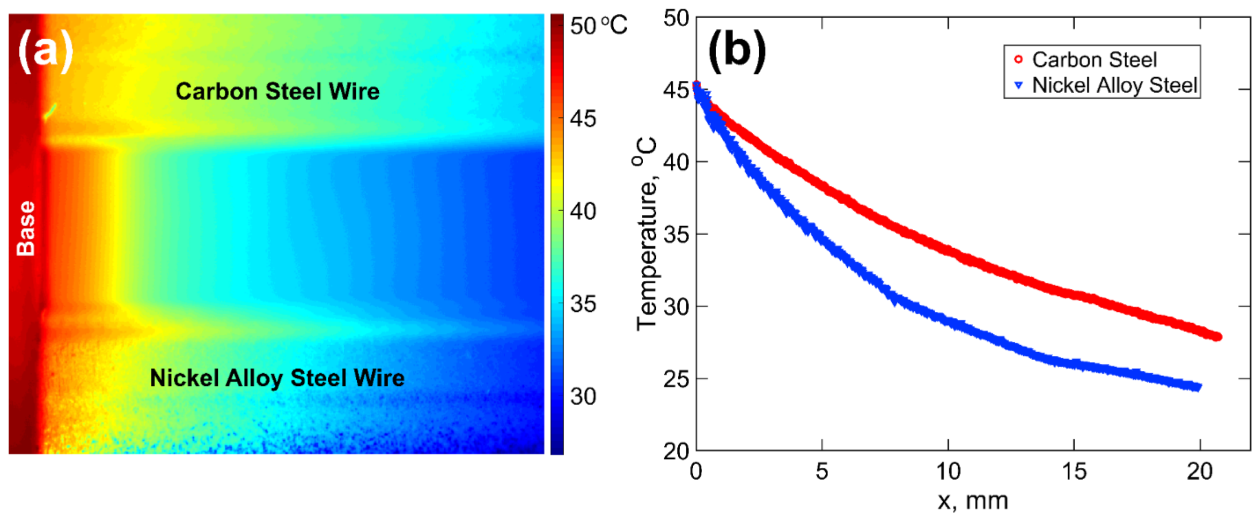

Figure 2 – (a) Raw steady-state infrared thermograph of two wires, carbon steel and nickel alloy steel, of diameters 3.16 mm and 3.18 mm respectively, (b) Steady-state temperature distribution along both wires.

2-4. Results and discussion

2.4.1. Temperature data and comparative determination of k_T

Figure 2(a) presents a raw thermal image at steady state showing simultaneous measurement on two wires – carbon steel (high strength 1045) and nickel alloy steel (thermally stable Invar 36). The wires are arranged parallel to each other with around 3.0 mm gap, and the wire base temperature is maintained at 45 °C. A clear temperature gradient down the wires can be observed for both materials. Temperature gradient normal to the wires is very small, indicating negligible wire-to-wire heat transfer. Figure 2(b) plots steady state temperature distribution along both wires, showing distinct, non-linear temperature gradient in each case, as expected from fin theory.

Further, Figure 3 plots temperature distribution on a semilog scale at a number of times prior to steady state for a 3.16 mm diameter stainless steel wire. These data show rapid changes in temperature distribution at early times as thermal diffusion from the base into the wire occurs. As time passes, a robust steady state distribution is established, with no significant temperature change beyond around 60 s. The steady-state temperature distribution is found to be linear on the semilog plot, as expected from equation (4). The slope of this curve may be used in accordance with equations (5) and (6) to determine unknown thermal conductivity of a test wire based on known thermal conductivity of a standard wire subjected to the same conditions.

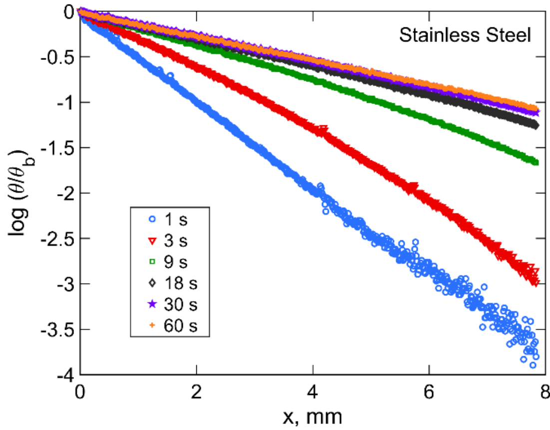

Figure 3: Temperature distribution at multiple times along a stainless steel wire showing establishment of a thermal steady state in approximately 60 s.

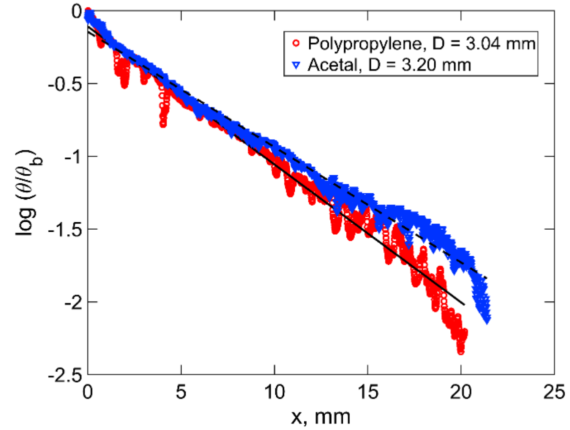

Figure 4: Measured temperature distributions in polypropylene and acetal wires of diameters 3.04 mm and 3.20 mm respectively. Data are plotted on a semilog scale, and linear curve fits are shown.

Note that linearity of the semilog plot shown in Figure 3 indicates the validity of the assumption that the heat transfer coefficient around the wire is independent of temperature. If there was significant temperature-dependence, equation (4) would not have been the correct temperature solution, and experimental data would not have resulted in a linear semilog plot of the temperature distribution. For further investigation of this, the wire temperature has been determined based on finite-element simulation as well as numerical solution of the governing energy equation assuming temperature-dependent convective heat transfer coefficient, and in each case, the results are found to be very close to those based on a constant value of the heat transfer coefficient.

Comparative experiments to determine thermal conductivity of a wire are summarized in Figures 4 and 5 for low thermal conductivity polymer wires and high thermal conductivity metal wires, respectively. Figure 4 plots $\log(\theta/\theta_b)$ vs x for two polymer wires – polypropylene and acetal – of around 3.0 mm diameters with base temperature of 35 °C. Plots for both wires shown in Figure 4 are linear, with R^2 value of greater than 0.97 in both cases. The slopes of both plots result in m =

94.76 m^{-1} and 79.31 m^{-1}, respectively. Thermal conductivity of polypropylene, separately measured to be 0.20±0.01 W/mK using a one-dimensional heat flux method described in Section 3, is treated to be a known, standard value. Based on equation (6), thermal conductivity of acetal is then determined to be 0.27±0.01 W/mK, which is within 3.6% of the independently measured value of 0.28±0.02 W/mK using the one-dimensional heat flux method. This demonstrates the capability of the measurement method to determine unknown thermal conductivity of a polymer wire based on known thermal conductivity of another wire.

In order to improve measurement accuracy, thermal conductivities of the standard and test wires must be of the same order of magnitude. Therefore, for thermal measurements on metal wires, the standard wire must have similarly high thermal conductivity. This is investigated in Figure 5 that presents experimental data for Aluminum (6061) and Copper (110) wires of around 3.0 mm diameter with a base temperature of 45 ºC. Unlike polymer wires, experiments for metal wires are carried out in the presence of forced convective cooling due to air flow at around 7.8 m/s from a fan. This is needed for metal wires in order to ensure a reasonable rate of decay of temperature along the wire and higher signal-to-noise ratio. Similar to polymer wires, linear temperature decay on the semilog plot is observed for metal wires, which is consistent with equation (4). The R^2 values are greater than 0.99 for both copper and aluminum wires. In this case, aluminum is treated as the standard wire. Thermal conductivity of a 25.4 mm diameter and 2.67 mm thickness sample machined from the same material as the wire is determined in advance using the laser flash method to be 182.7±9.1 W/mK. Based on this, thermal conductivity of the copper wire is determined using equation (6) to be 401.5±26.5 W/mK. This compares well with an independent laser flash measurement of 403.2±20.2 W/mK as well as the manufacturer-specified value of 390.9 W/mK.

Figures 4 and 5 together demonstrate the capability of the method described in Sections 2 and 3 to accurately measure thermal conductivity over a wide range of values, covering both low thermal conductivity materials such as polymers and high thermal conductivity materials such as metals.

A series of additional measurements are also carried out for both polymers and metals, using different materials as standard. These data are summarized in Tables 1 and 2 for metal and polymer materials, respectively. Very good agreement with independently measured or manufacturer-provided values for thermal conductivity are observed in each case, thereby demonstrating the versatility of the measurement method. Note that Aluminum is used as standard for relatively high thermal conductivity metals, while Carbon Steel is used as standard for relatively low thermal conductivity metals. Thermal conductivity of both Aluminum and Carbon Steel are measured independently using laser flash method.

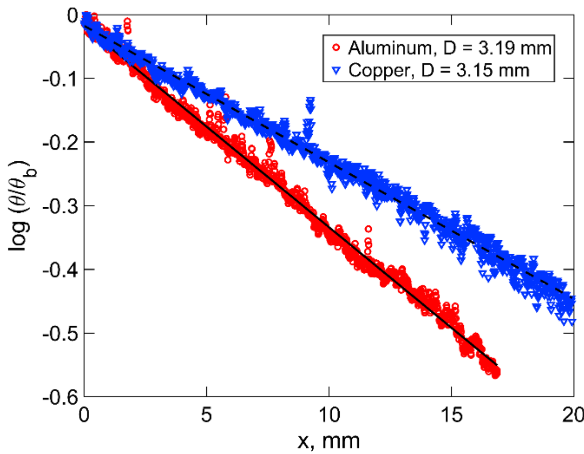

Figure 5: Measured temperature distributions in aluminum and copper wires of diameters 3.19 mm and 3.15 mm respectively. Data are plotted on a semilog scale, and linear curve fits are shown.

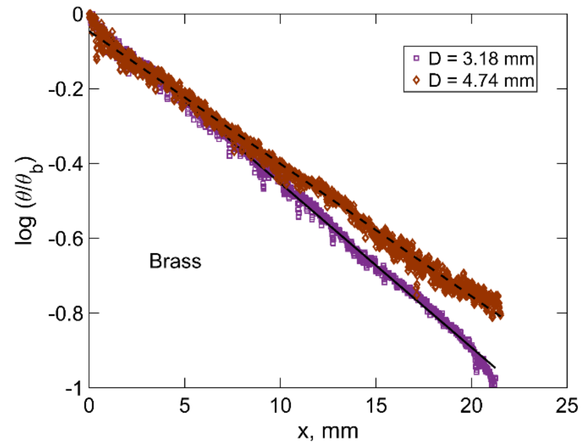

Figure 6: Comparison of temperature distributions of two Brass wires of significantly different diameters (3.18 mm and 4.74 mm), showing consistency with theoretical model.

2.4.2. Measurements on wires of different diameters

As shown in equation (4), wire size plays a key role in determining the value of m, and hence in the measurement of thermal conductivity. Figure 6 plots $\log(\theta/\theta_b)$ vs x for two wires of the same material – Brass (360) – but different diameters. As expected, the rate of temperature drop is greater for the thinner wire due to larger value of m for smaller diameter wires. Equation (5) shows that for wires of different diameters but the same material and ambient conditions, the non-dimensional product $D\times m^2$ must be constant. This product is found to be 6.13 and 5.95 for the 3.18 mm and 4.74 mm wires, respectively. These values are within 2.9% of each other, indicating that the nature of heat transfer during these experiments is consistent with the theoretical model presented in Section 2. Note that the convective heat transfer coefficient h for two wires of different diameters may be somewhat different even when subjected to the same ambient conditions. This is because convective heat transfer from a heated wire is, in general, a function of the wire diameter. In the case of forced convection, as the wire diameter increases, convective heat transfer coefficient decreases [35], and therefore, m reduces. Similarly, natural convection heat transfer coefficient also depends on the wire diameter. Based on well-known correlations for convective heat transfer from cylinders [33–35], it is found that for natural convection, this is not a significant effect around 2-6 mm diameter wires in air. On the other hand, for forced convection, this is not a significant effect for wires greater than around 2 mm diameter in air. Therefore, within these ranges, choosing different diameters for the test and standard samples may be acceptable, whereas outside these ranges, it may be important to closely match the diameters of the test and standard wires.

Table 1: Summary of measurements on a variety of metal wires using aluminum and carbon steel wires as standard.

Standard Wire			Test Wire				
Material	Diameter, mm	Thermal Conductivity, W/mK	Material	Diameter, mm	Thermal Conductivity, W/mK		
					Measurement	Manufacturer-provided value	% Deviation
Aluminum	3.19	182.7±9.1 (Laser Flash)	Copper	3.15	401.5±26.5	390.9	+2.7
			Carbon Steel	3.16	49.1±3.03	50.4	-2.7
			Brass	3.18	110.3±6.9	115.0	-4.1
Carbon Steel	3.16	45.8±2.3 (Laser Flash)	Alloy Steel	3.16	43.0±2.6	43.2	-0.5
			Stainless Steel	3.16	14.1±0.9	14.4	-2.5
			Nickel Alloy	3.18	11.0±0.7	10.1	+8.3

Table 2: Summary of measurements on a variety of polymer wires using polypropylene and PVC wires as standard.

Standard Wire			Test Wire				
Material	Diameter, mm	Thermal Conductivity, W/mK	Material	Diameter, mm	Thermal Conductivity, W/mK		
					Measurement	Independently measured value	% Deviation
Polypropylene	3.04	0.20±0.01 (Heat flux method)	Acetal	3.20	0.27±0.02	0.28	-3.6
PVC	3.05	0.14±0.01 (Heat flux method)	ABS	3.02	0.14±0.01	0.13	+3.3
			PTFE	3.24	0.16±0.01	0.17	-2.6

Figure 7 presents data for an even more general case where the two wires have different diameters and are of different materials. Specifically, carbon steel and stainless steel wires of diameters 3.16 mm and 4.77 mm respectively are used, treating carbon steel as the standard wire with a known thermal conductivity of 45.8±2.3 W/mK based on aluminum wire as reference. As

shown in Figure 7, linear semilog plots are obtained in this case, similar to prior experiments. Based on the *m* values determined from the temperature measurement and taking into account the unequal diameters of the wires, thermal conductivity of the stainless steel is found to be 14.1±0.9 W/mK, which is within 2.5% of the manufacturer-provided thermal conductivity of 14.4 W/mK.

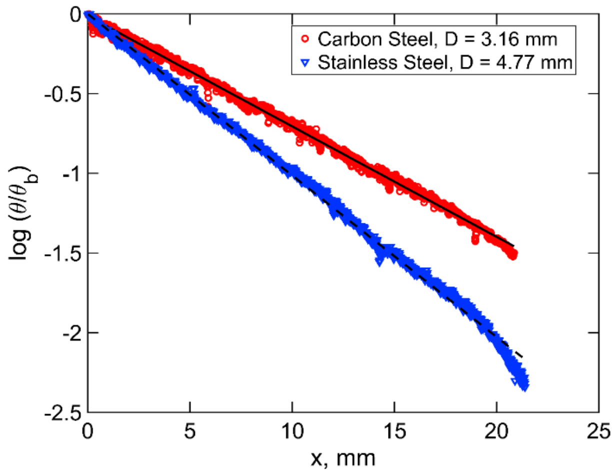

Figure 7: Comparison of temperature distributions of two wires of different materials and diameters (Carbon Steel, 3.16 mm and Stainless Steel, 4.77 mm)

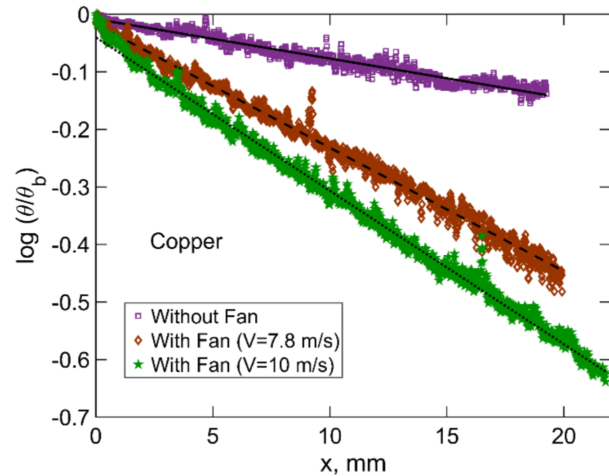

Figure 8: Measured temperature distributions for the same copper wire of 3.15 mm diameter in three different convective cooling conditions.

2.4.3. Impact of experimental conditions on measurement accuracy

Figure 8 examines the effect of external air flow on the measurements. Measured temperature distributions for the same 3.15 mm diameter copper wire subjected to three different convective cooling conditions are presented. These include natural convection and forced convection at two different fan speeds. As expected, there is greater rate of temperature reduction with increased air flow. In each case, the temperature distribution is found to be linear on the semilog plot, consistent with equation (4). The values of *h* for these three cases obtained by data fitting and based on the known thermal conductivity of the copper wire are found to be 14, 135

and 209 W/m^{2}K, respectively, which, as expected increase with fan speed. While it is not claimed that the heat transfer coefficient can be measured in this manner, these data demonstrate consistency between experimental measurements and the theoretical model discussed in Section 2.

The effect of base temperature on the measurements is examined next. Theoretically, the base temperature is not expected to influence measurements, since it does not impact the slope m of the $\log(\theta/\theta_b)$ vs x plot. However, a low base temperature results in low overall temperature rise in the wire, leading to greater noise relative to the higher wire temperature rise. In order to examine this effect, temperature distribution for a 3.15 mm diameter copper wire is plotted for three different base temperatures in Figure 9, keeping convective cooling conditions the same. It is observed that greater base temperature results in significant reduction in noise. The higher the base temperature, the greater is the R^2 value of the linear fit, and thus the greater is the accuracy in thermal conductivity measurement. However, the base temperature should not be so large that secondary effects such as radiative heat transfer and natural convective motion due to the hot base become important. This is an important consideration since natural convection close to the base may result in axially varying convective heat transfer coefficient, which is not captured by the analytical model presented here. Further, for measurements of thermal conductivity as a function of temperature, the temperature range in each measurement must be designed to be as low as possible, while still ensuring reasonable signal-to-noise ratio. Such trade-offs are important to consider for effective design of a thermal conductivity measurement experiment based on the technique discussed in this project.

2.4.4. Measurement of thermal conductivity of solder wires

Finally, in order to demonstrate the application of this technique, thermal conductivities of a variety of solder wires are measured. 3.16 mm diameter carbon steel wire is used as the standard wire for each solder wire measurement. Table 3 summarizes the measurement results for machine solder, solder for drinking water, torch solder and rosin flux core solders. Note that both torch solder and rosin flux core solders have the same outer diameter and composition of 60% Lead and 40% Tin. However, the rosin flux core solder has an inner core of flux material, with the solder material forming an annular ring. The measured thermal conductivities of 40.6±2.6 W/mK and 31.3±2.0 W/mK are consistent with the material composition, as the presence of low thermal conductivity flux material is expected to result in lower thermal conductivity of the rosin flux core solder wire. The thermal distinction between the two wires is also clear from the comparative thermal measurement shown in Figure 10.

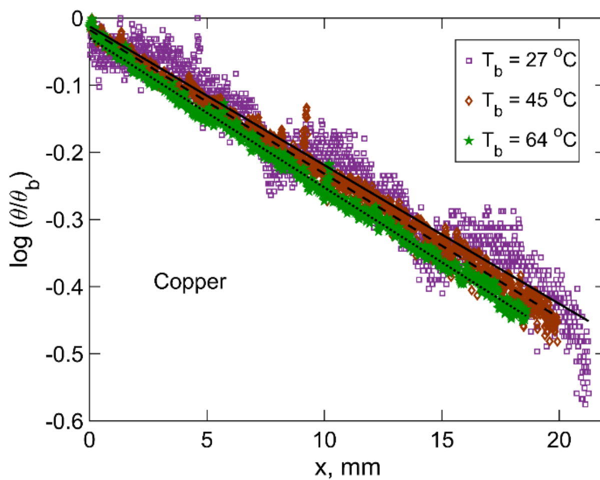

Figure 9: Measured temperature distribution for the same copper wire of 3.15 mm diameter with three different base temperatures. This plot shows

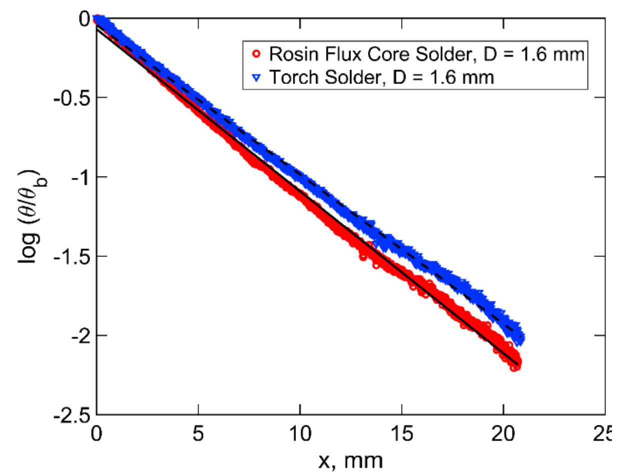

Figure 10: Measured temperature distributions in rosin flux core solder and torch solder wires of diameters 1.6 mm each. Data are plotted on a semilog scale, and linear curve fits are shown.

the impact of base temperature on noise in the measured data.

2.4.5. Validity of infinite fin assumption

A key assumption made in the theoretical model presented in Section 2 is that the wire is infinitely long. This assumption facilitates derivation of the temperature distribution, equation (4), without needing to know the thermal state of the fin tip. In order to verify the appropriateness of the infinite fin assumption for wires investigated in this work, temperature distribution for the entire length of two representative wires – one polymer and the other metal – are plotted in Figure 11. These data clearly show that for both wires, temperature reduces to the ambient temperature within the wire length, thus showing that the infinite fin assumption is applicable. Note that even though the choice of the overall wire length is dictated by the infinite fin assumption, measurement of thermal conductivity is based on temperature rise in only a shorter section of the wire, typically the first three quarter-lengths of the wire, where the temperature rise is reasonably large. Beyond this length, temperature rise is found to be small/noisy, and is, therefore, neglected for determining thermal conductivity.

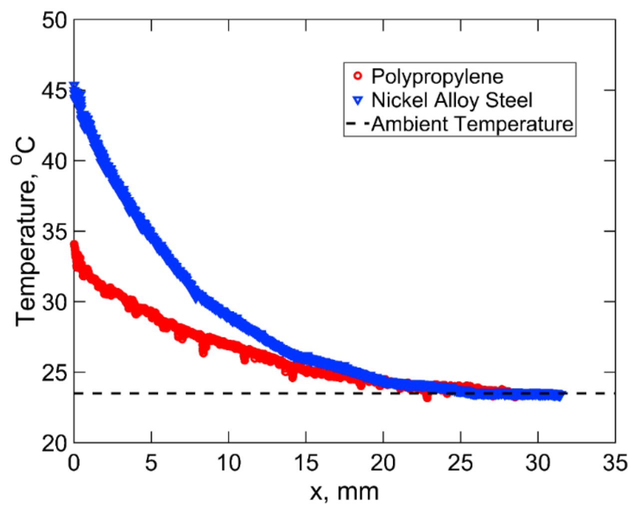

Figure 11: Temperature distributions in the entire length of polypropylene and nickel alloy steel wires for the validation of infinite fin assumption.

2.4.6. Uncertainty analysis

Error propagation analysis is carried out in order to estimate the uncertainty in thermal conductivity measurements reported here. Differentiating equation (6) results in

$$\frac{\partial k_T}{k_T} = \frac{\partial k_S}{k_S} + \frac{\partial D_S}{D_S} + \frac{\partial D_T}{D_T} + 2\frac{\partial m_S}{m_S} + 2\frac{\partial m_T}{m_T} \tag{8}$$

The relative error in measurement of the thermal conductivity of standard wire material, based on laser flash technique and one-dimensional steady state heat flux methods described in section 3.3, is estimated to be 5% and 4% respectively, based on manufacturer specifications. Uncertainty in measurement of wire diameter is estimated based on the least count of 0.01 mm of the Vernier caliper used. Finally, uncertainties in the slopes m_S and m_T may occur due to error in infrared temperature measurement. A linear regression analysis of the measured temperature distribution along the wire, accounting for the manufacturer-specified maximum error in infrared temperature measurement, is carried out. This is found to be result in an uncertainty of less than 0.25% for metals and 0.40% for polymers in each slope. Combining all of the uncertainties, the uncertainty in measurement of thermal conductivity of the test wire is estimated to be around 6.1% for the case of acetal based on polypropylene. Similar uncertainties are estimated for other measurements as well and are listed in Tables 1-3.

Note that once the thermal conductivity of a wire has been measured by comparison against a standard wire, the wire can, in principle, then be used a standard wire to measure thermal conductivity of other wires as well. However, this is not recommended since this may lead to significant uncertainty propagation through both experiments. Thermal conductivity of the standard wire must always be determined through an independent measurement. Only when an

independently measured wire is not available for use as standard, should a previously measured wire be used as a standard, and even then, in doing so, one must recognize the possibility of increased measured uncertainty.

Table 3: Summary of measurements on a variety of solder wires using Carbon Steel wire as reference, for which a thermal conductivity of 45.8 W/mK is independently measured using LFA technique.

Material	Composition	Diameter, mm	Measured Thermal Conductivity, W/mK
Machine Solder	Lead (70%), Tin (30%)	3.26	41.3±2.5
Solder for Drinking Water	Lead (0%), Tin (95%), Copper (4.8%), Silver (0.2%)	2.96	42.4±2.5
Rosin Flux Core Solder	Lead (60%), Tin (40%)	1.6	31.3±2.0
Torch Solder (without Flux)	Lead (60%), Tin (40%)	1.6	40.6±2.6

2-5. Nomenclature

A_c	Cross-sectional area, m^2
D	Diameter, m
h	Convective heat transfer coefficient, W/m^2K
k	Thermal conductivity, W/mK
L	Sample thickness, m
l	Length, m
m	Slope of semilog plot of temperature distribution, m^{-1}
P	Perimeter, m
T	Temperature, K
t	Time, s
x	Spatial co-ordinates, m
α	Thermal diffusivity, m^2/s
θ	Temperature rise, K

Subscripts

a	Ambient
b	Base
max	Maximum
S	Standard wire
T	Test wire

Chapter 3

Detection of Unusual Thermal Activities in a Semiconductor Chip using Backside Infrared Thermal Imaging

Published as: Salvi, S. S., Jain, A., "Detection of unusual thermal activities in a semiconductor chip using backside infrared thermal imaging", *ASME Journal of Electronic Packaging*, Vol. **143**(2), pp. 020901:1-8, 2021.

3-1. Introduction

The security of modern microprocessors and other semiconductor chips is of critical importance, particularly for sensitive applications, such as defense, finance, etc. Due to the highly distributed nature of design, manufacturing and assembly, semiconductor chips have become increasingly vulnerable to hardware and software Trojans. A hardware Trojan is any unidentified circuit that can access, distort or disable ongoing operations anonymously [38]. The intended or unintended introduction of an undesired circuit element could occur, for example, at an external foundry or chip packaging company that simultaneously serves multiple clients across the globe. A software Trojan could be introduced in a network attack on the chip. Even though a software Trojan does not involve physical alterations in the chip, it can have similarly deleterious effect on chip operation. Rapid detection and disablement of Trojans – both hardware and software – is a critical security need for semiconductor chips [39,40].

Trojan detection is inherently challenging due to the stealthy nature of the Trojan, the behavior or characteristics of which are not known in advance and may change over time [41]. Accuracy, cost and speed of detection are key figures of merit for any Trojan detection approach. A good detection technique must minimize the likelihood of false negatives – when the detection method fails to identify a Trojan-related activity – and false positives – when an activity is detected to be Trojan-related, but is, in fact, benign.

While a hardware Trojan may, in principle, be detected using destructive testing and reverse engineering, such an approach is expensive, time consuming and unlikely to be practical [42]. Several non-destructive methods have been proposed for Trojan detection. These methods can be broadly categorized into side-channel analysis and full Trojan activation, also known as

logic testing method [43]. Side-channel analysis methods track changes in circuit parameters such as impendence, current or power [40,44,45], path delays [46,47], surface temperature [48], etc. which are generally a side effect of Trojan activity. The efficacy of side channel analysis depends on the magnitude of side-channel signal generated by the Trojan, which malicious players strive to keep to a minimum [39]. Logic testing methods are used to enhance the side-channel analysis method, by finding the set of test vector patterns that, when applied to the chip, maximizes the probability of activating available hardware Trojans [49].

Side-channel analysis based on current, or power measurements determine and compare the circuit power ratio to that of a known, trusted chip, also called as a golden IC [50]. The need for a golden IC can be eliminated by comparing IC current signatures at two different times to detect abnormal patterns and spot a hardware Trojan [44]. Path delay-based side-channel analysis methods work on generating and detecting anomalies in path delay [46,47]. The key benefit of this approach is that the Trojan does not even need to be activated for detection [51]. On-chip sensors have also been used for detecting side channel signals [52,53], including current/power sensors [54,55] and delay counters [56,57]. Side-channel signal measurements such as localized electromagnetic emanation [58] have also been used to detect unusual patterns due to hardware Trojan activation. Synergistic combination of multiple side-channel signals has been investigated. For example, combination of current with delay [59], current with maximum frequency [41] and time with electromagnetic measurements [60] has been shown to offer improved detection than analysis based on only one signal. The logic testing approach has also been used in conjunction with side-channel analysis to improve the performance of signal measurements and improve the accuracy of Trojan detection [41,61].

Infrared (IR) based thermography has traditionally been used in the semiconductor industry for surface temperature measurement [62,63], detecting defective chips [64], hotspot detection [65,66], etc. In principle, Trojans are intended to draw minimal current and remain undetected. Nevertheless, abnormal circuit activity due to a Trojan is expected to cause some distortion in the temperature field of the chip due to Joule heating. Some literature is available on the use of this thermal signal for hardware Trojan detection using infrared imaging and image processing approaches. In general, the temperature field from an IR camera is represented as time-varying matrices, which are analyzed for detecting a hardware Trojan. 2-D principal component analysis has been used to calculate and compare the Euclidean distance for the test chip and a benchmark chip [42]. Unsupervised clustering methods have been used for hardware Trojan detection without the need for a benchmark chip [67]. Similarly, application of Kalman filters on the difference matrices of IR thermal images at two different time periods has been used for hardware Trojan detection [68,69]. Most of this past work pertains to traditional, planar chips. In contrast, detection on a 3D IC – which refers to a stack of multiple die that are electrically interconnected with each other – have not been investigated much.

This project presents measurement of temperature field of the transistor plane of a two-die 3D IC thermal test chip through infrared imaging from the backside of the top chip. Due to the infrared-transparent nature of bulk Silicon and infrared-opaque nature of insulation layers above transistors, this facilitates direct thermal imaging of the transistor plane. The occurrence of unusual thermal activities mimicked through Joule heating in embedded metal resistors is detected through image analysis. The performance of a number of image analysis algorithms is benchmarked and compared. While past work is available on temperature-based detection in traditional, planar chips, the present work specifically investigates a two-die 3D IC and suggests possible mechanisms for

improved Trojan detection in a 3D IC. Results from this work can be utilized to develop improvised real time algorithms for quick and effective Trojan detection techniques.

3-2. Experimental Setup

Experiments are carried out to investigate the use of backside infrared thermal imaging to predict the onset of Trojan-related unusual activity on the chip. For these experiments, a two-die, three-dimensional integrated circuit (3D IC) is used [70]. Figures 12(a) and 12(b) show top view and cross-section view schematics of the 3D IC. This 3D IC has two unequally sized die bonded face-to-face to each other. Each chip has two embedded metal resistors of around 500 Ω each on the M7 layer. Figure 12 shows schematic top and cross-section views of the 3D IC used in this work. The 3D IC is bonded on to a leadless chip carrier substrate such that the backside of the top die is optically accessible. I/O pads on the periphery of the larger-sized, bottom chip are wire bonded to bond pads on the substrate. The substrate is, in turn, mounted on a ceramic socket. This enables electrical access to various features on both die of the 3D IC. A Keithley 2602B power source is used for passing current through the metal resistors on each die.

Figure 13(a) shows a picture of the experimental setup, including the two-die 3D IC packaged in a chip carrier and socket. Figure 13(b) shows a close-up view of the 3D IC. A FLIR A6703sc IR camera with 640 × 512 pixel resolution and 15μm pixel pitch is used. Infrared emission is measured at 100 Hz frequency and converted to temperature field. The camera is mounted to focus on the bare backside of the top chip of the 3D IC. Infrared data are acquired using ResearchIR software and analyzed using MATLAB. Temperature maps obtained from emissivity field measurements are stored in the form of matrices A_n, where n depicts the time step. The backside of the top chip is not coated with graphite, because in this case, the interest is in

imaging temperature distribution on the transistor plane, and not the chip backside. By not having an IR-opaque graphite layer on the backside – as is customary for surface IR thermography – the IR camera in this case is able to directly measure the temperature field on the transistor plane instead of the backside temperature. The impact of a graphite layer on the die backside is discussed in more details in Section 4.4.

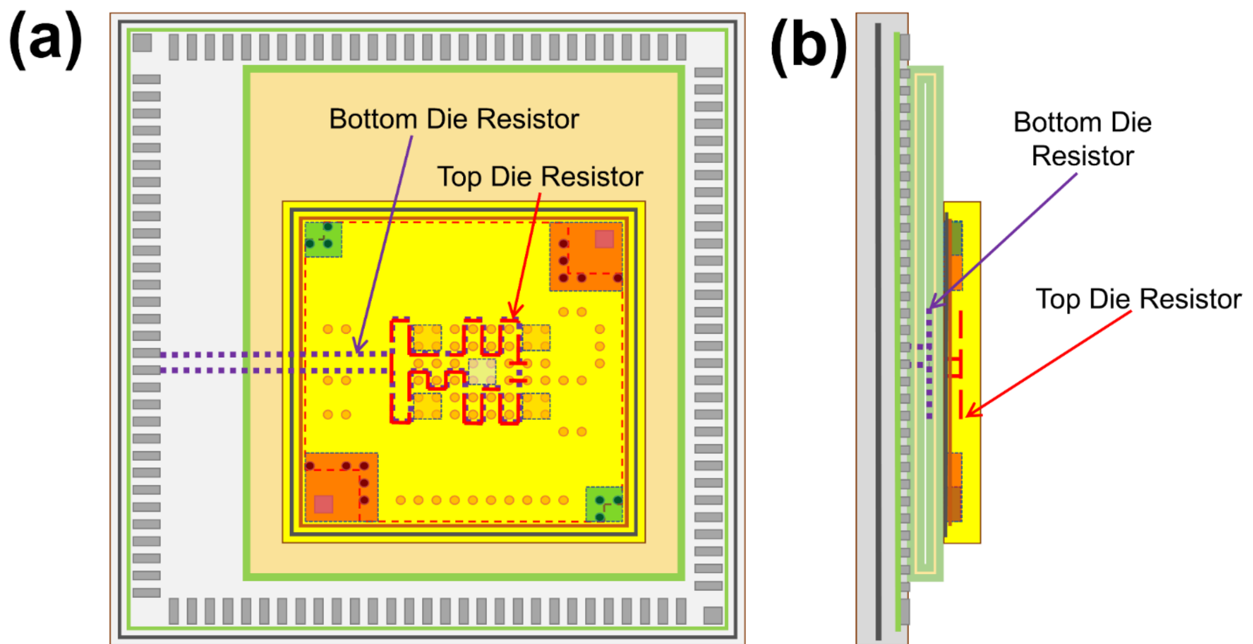

Figure 12. Schematic picture of the two-die 3D IC used in this work. (a) and (b) show top and cross-section views, respectively.

The thermal effect of Trojan activity is mimicked through Joule heating in independently addressable top and bottom die resistors in the thermal test chip, as shown in Figure 12. The use of Joule heating that mimics a hardware Trojan on either the top or bottom die of the 3D IC facilitates analysis of different possible Trojan activity levels. Experiments are carried out to investigate a variety of Trojan activity scenarios, which includes variations in heating current from 0.1mA to 25 mA for the resistors in the top and bottom die. In each case, the capability of detection, including speed, accuracy and occurrence of false positives and negatives is investigated.

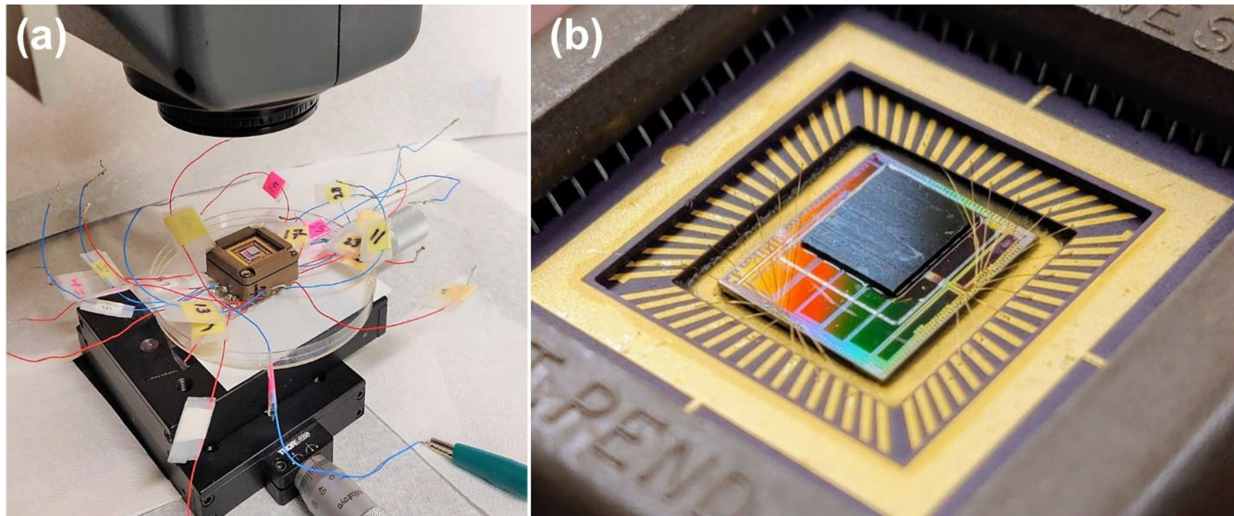

Figure 13. Picture of the experimental setup. (a) shows the packaged 3D IC under the infrared camera and connected to an external power source; (b) shows a close-up view of the 3D IC – the two unequally-sized die and wire bonds from the bottom die to the chip carrier are visible. In this configuration, the top-most surface of the 3D IC is the backside of the top die, through which, infrared thermography is carried out.

3-3. Image Processing Techniques

Figure 14 shows a schematic of the data acquisition and analysis framework used in this project. Following image acquisition as described in Section 2, the data at various times are analyzed using four image processing algorithms. Background subtraction, binary conversion and filtering is also carried out. The performance of a variety of image process algorithms for such detection is characterized and compared. The fundamental premise behind anomaly detection is to compare successive thermal images in time with the ultimate thermal image of the chip – also called the standard image – in response to a thermal load and determine the minimum time at which the degree of similarity between the two exceeds a certain threshold. A comparison of the performance of these algorithms is carried out in terms of minimum detection time, occurrence of false positives and false negatives, etc.

A brief summary of the four image analysis algorithms used in this work is presented below:

3.3.1. Binary comparison method

In this method, the temperature field is converted into a binary signal based on comparison with a threshold value of the temperature. The threshold is chosen to be 0.55 times the average of ten highest temperature values. Image comparison is then carried out between the binary equivalents of the image matrix under consideration and the standard image matrix. The percentage similarity between the two is defined as the percentage of pixels with a binary one entry in the term-by-term product of the two matrices.

3.3.2. Structural similarity (SSIM) index method [71]

SSIM quantifies the similarity between two images by using three factors for comparison - luminance, contrast and structure [71]. The SSIM index is calculated to be [72]

$$\mathrm{SSIM}(A,B) = \frac{(2\mu_A\mu_B + C_1)(2\sigma_{AB} + C_2)}{(\mu_A^2 + \mu_B^2 + C_1)(\sigma_A^2 + \sigma_B^2 + C_2)} \quad (9)$$

Where, A and B are the two images to be compared, and μ_A, μ_B, σ_A^2, σ_B^2, σ_{AB} are means for A and B, covariances for A and B, and the covariance between A and B, respectively. C_1 and C_2 are constants that are included to avoid instability [73]. A high value of SSIM calculated using equation (9) represents a large degree of similarity between the images being compared.

3.3.3. 2-D correlation coefficient method [74]

The 2D correlation method compares the magnitudes and locations of peaks between the test and standard images. Specifically, the zero-normalized cross correlation is calculated as follows [74]

$$\mathrm{corr}_2 = \frac{\sum_i \sum_j (f_{i,j} - f_\mu)(g_{i,j} - g_\mu)}{\sqrt{(\sum_i \sum_j (f_{i,j} - f_\mu)^2 \, (\sum_i \sum_j (g_{i,j} - g_\mu)^2)}} \tag{10}$$

Where, $f_{i,j}$ and $g_{i,j}$ are the two datasets to be compared and f_μ and g_μ are the averages of corresponding datasets. Similar to SSIM, the 2-D correlation coefficient also represents a degree of similarity, although the specific values of the two parameters may differ. This correlation technique has been used in applications such as measurement of strain [74] and in-plane deformation [75]

3.3.4. Histogram comparison method [76]

In this method, a vector, or histogram, containing the distribution of discrete pixel intensities of the differential thermal image is computed and used as the basis for comparison between a reference and test differential image [76]. The degree of similarity, defined as the average pairwise distance between the histograms of the two images, is computed. This pairwise distance is the difference between the probability density at every normalized pixel intensity for the two histograms plotted. Higher the pairwise distance, lower is the degree of similarity of test image against reference image. This approach is illustrated in Figure 15, which plots the probability density as a function of normalized pixel intensity for a reference image (no heating in the circuit) and a test image (10 mA current passing through the top die resistor). This Figure plots the number of pixels that correspond to a specific pixel intensity value. Both are plotted in

normalized form. This figure shows, as expected, that the image for dead circuit has higher number of pixels with low intensity, i.e., less than 10% intensity, than the test image with active top die resistor. The histogram for test image appears to be normally distributed in the range of 0% to 35% of pixel intensity. Simulated hardware Trojan in active state produces heat due to joule effect and thus it will surely tweak with the pixel intensity configuration of infrared image of the circuit, which can be easily traced by this method. Thus, sudden change in intensity of successive images will trigger the similarity index which can be used to identify the Trojan activity.

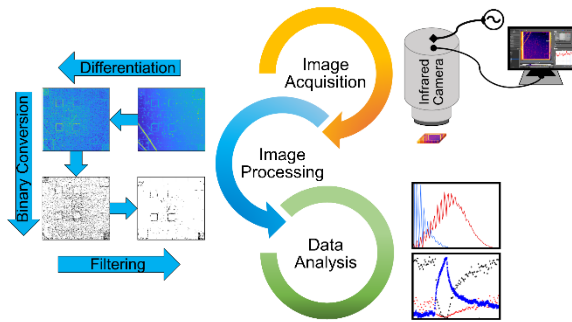

Figure 14 – Schematic of the computational framework used for data acquisition and analysis.

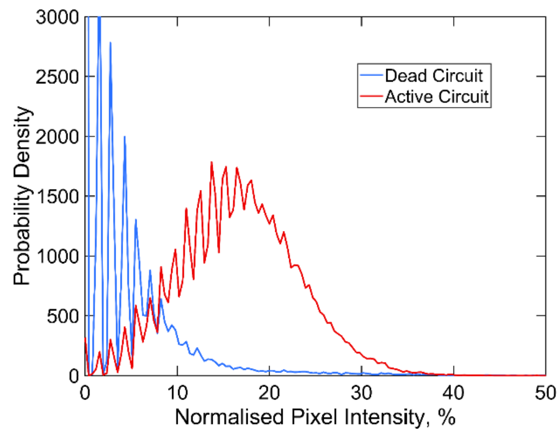

Figure 15 – Pixel probability density as a function of pixel intensity, as an illustration of the histogram comparison method

3-4. Results and Discussion

3.4.1. Temperature colormaps

Figures 16(a) and 16(b) present representative temperature colorplots at different times obtained from infrared imaging for experiments with 15 mA and 5 mA heating current through the top die resistor. In each case, measured temperature map at t=0 s prior to passing the current is subtracted. In the 15 mA case shown in Figure 16(a), a distinct signal is clearly detected even at

0.1 s, with the signal becoming more and more distinct at larger times. For the lower, 5 mA current case shown in Figure 16(b), a similar detection is not visible as clearly at t=0.1 s but emerges much later due to the weaker heat generation. Figure 17 plots the average measured temperature rise as a function of time for multiple heating currents passing through the top die resistor. It is seen that the expected temperature rise for 5 mA and lower currents is quite low. While the distinction between the 15 mA and 5 mA cases can be seen visually in Figure 16, quantitative signal processing methods are clearly desirable for systematic, real-time data analysis and Trojan detection, particularly at low activity levels.

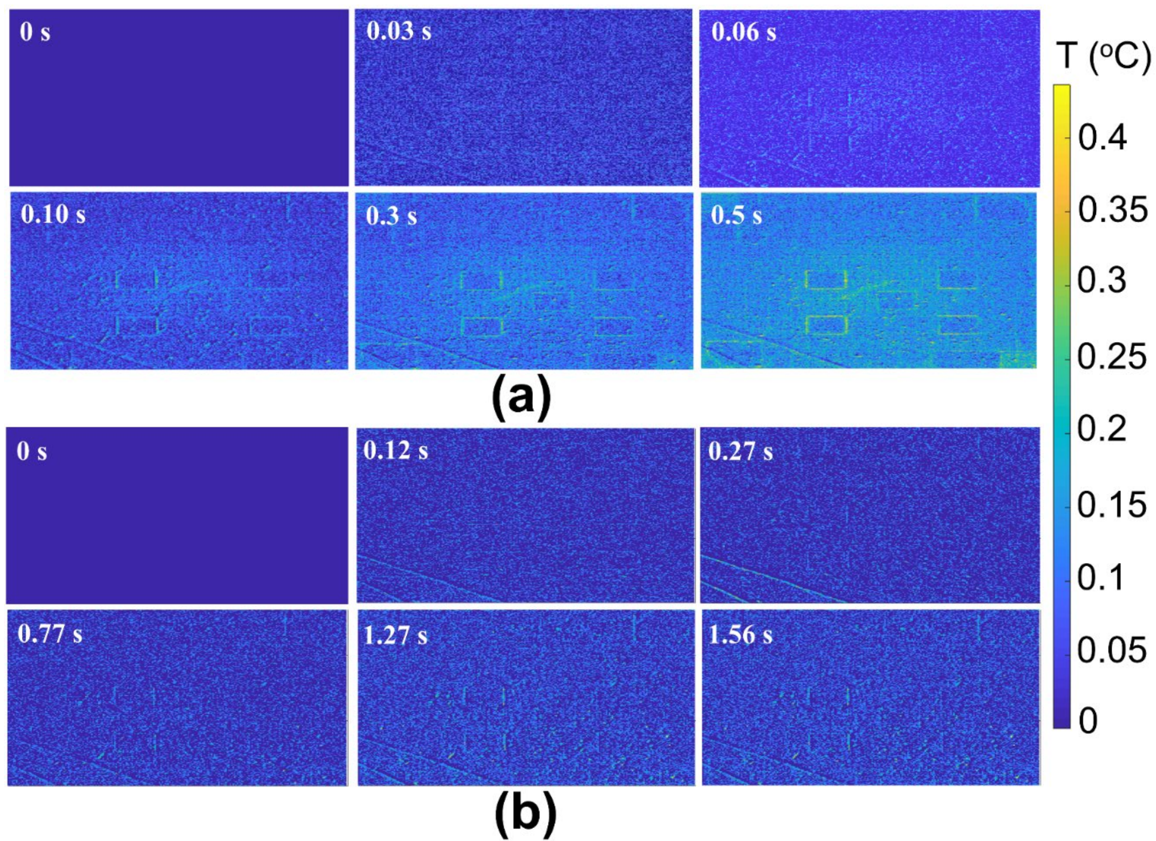

Figure 16 – Measured temperature maps on the top die, in response to (a) 15 mA, and (b) 5 mA heating current in the top die resistor. Temperature maps are differential, after subtracting a baseline image prior to onset of heating.

3.4.2. Algorithm-based detection with top die resistor activated

The four image analysis algorithms discussed in Section 3 are applied on the differential images acquired from experiments with different currents passing through the top die resistor. Figures 18(a) and 18(b) plot the degree of similarity as a function of time for the four image analysis algorithms at 15 mA and 5 mA heating currents, respectively.

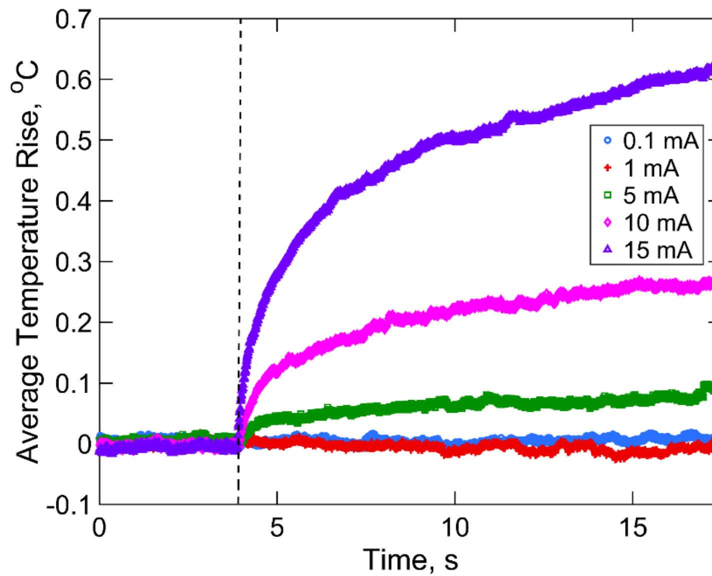

Figure 17 – Measured average temperature rise as a function of time for a number of heating currents in the top die resistor.

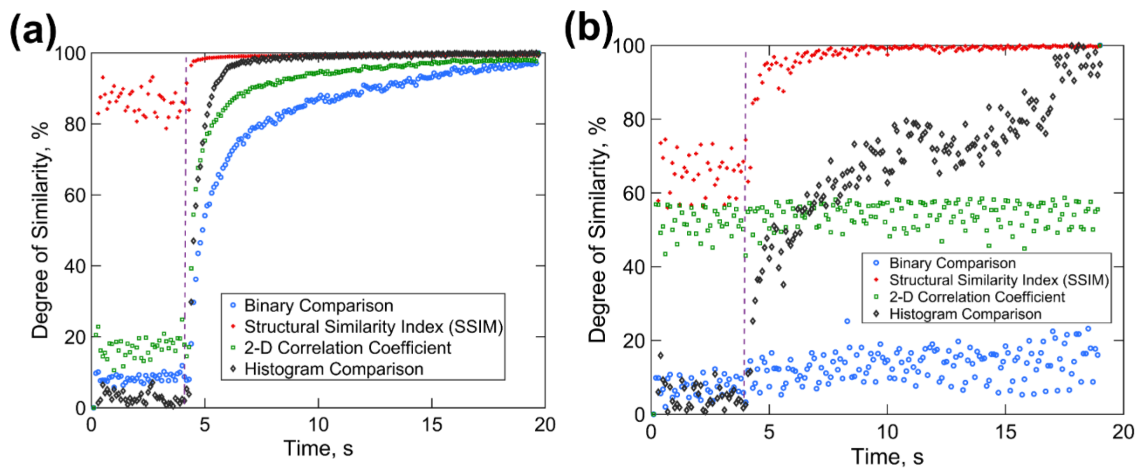

Figure 18 – Degree of similarity predicted by four different image processing algorithms as a function of time when the top die resistor is activated with (a) 15 mA, and (b) 5 mA current.

In the case of 15 mA case, each method exhibits sharp rise in the degree of similarity just after current activation. The histogram comparison approach reports the most rapid change in degree of similarity. On the other hand, the degree of similarity reported by SSIM method is relatively high even prior to current activation, due to which, the relative change in signal may be low.

Detection of a 5 mA signal – corresponding to only 12.5 mW power – is more challenging due to the lower heating rate. This case is shown in Figure 18(b). In this case, the binary comparison and 2-D correlation coefficient method fail to detect the onset of the heating activity – the predicted degree of similarity does not change appreciably following the onset of heating. On the other hand, the SSIM index and histogram comparison method work much better and show a sharp increase in the degree of similarity. A key trade-off between the two is that while the SSIM method jumps to 100% similarity faster, it does exhibit a high degree of similarity even prior to the onset of heating activity. This might cause SSIM to report more false negatives. On the other hand, histogram comparison method is much slower to report 100% similarity, but provides a greater contrast compared to the pre-heating measurement. As a result, the histogram comparison method may take longer and may report more false negatives, especially if the time window available for detection is short, but may be more immune to false positives. The final choice between the two algorithms may depend on the relative importance of fast detection and avoiding false positives/negatives in the specific application. It is possible that a hybrid evaluation that combines both methods could be employed to meet detection needs across this spectrum of requirements.

For further comparison of the four algorithms, experiments are repeated at a number of currents, up to 25 mA in the top die resistor. Figure 19 compares performance of the image analysis algorithms as a function of heating current. Figure 19 plots the mean difference in degree of similarity before and after starting the heating current in the top die. This allows comparison of the algorithms on a scale with same starting point. Higher mean difference in degree of similarity confirms a strong signal for identifying unusual thermal activities for a particular technique at a specific input current. Figure 19 shows that the use of binary comparison and 2D correlation coefficient method may not be effective for the detection of unusual thermal activities at lower signal. On the other hand, SSIM index and histogram comparison methods work well for small signals. The histogram comparison method exhibits a high difference in degree of similarity over the entire range of thermal signals, whereas the SSIM index method does saturate after a certain amount of current.

It is instructive to compare how the degree of similarity and average temperature rise change as functions of time. This is plotted in Figure 20 for 5 mA heating in the top die resistor, i.e., carrying as less as 12.5 mW power. Data on degree of similarity are plotted only for SSIM and histogram comparison methods, since these appear to be more effective than the other two methods. The vertical dashed line represents the time at which the top die resistor is triggered. Figure 20 shows the even though the temperature rise may be very small (less than 0.1 ºC), SSIM and histogram comparison methods are able to detect the thermal activity very quickly.

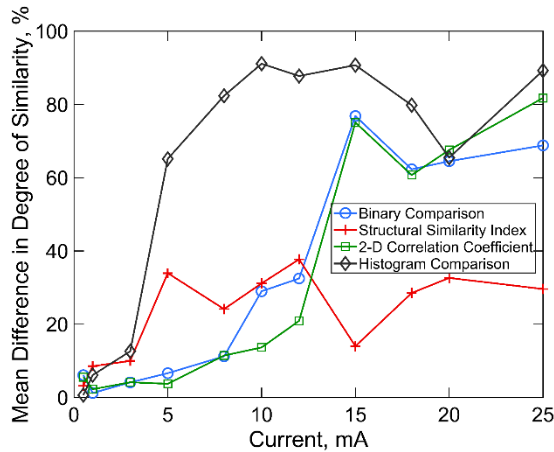

Figure 19 – Mean difference in degree of similarity before and after heating event for a number of heating current. Data are shown for four different image process algorithms.

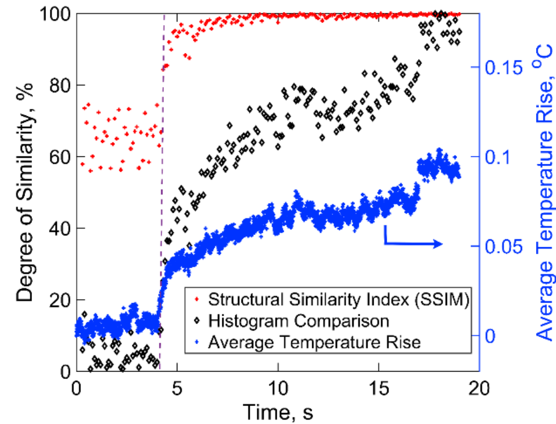

Figure 20 – Measured average temperature rise and degree of similarity plotted as functions of time for 5 mA heating current through the top die resistor. Data are shown for SSIM index and histogram comparison methods.

3.4.3. Algorithm-based detection of heating pulse with background thermal activity

The set of experiments discussed is section 4.2 imposed a heating current on the top die resistor representative of Trojan activity, while the remaining chip is inactive. Also, the heating current stayed on throughout the experiment. In realistic conditions, Trojan activity must be detected in the presence of background thermal activity due to legitimate processes, and, in addition, the Trojan activity may last only a short time. To investigate the impact of these realistic considerations on detection accuracy, experiments are carried out where a single pulse of 10 mA current and 1 s duration is passed through the top die resistor to represent Trojan activity, while the bottom die resistor is either kept inactive, or is active with 10 mA current. Figure 21 (a) and (b) plot the degree of similarity using SSIM index and histogram comparison methods as well as average temperature rise for these two scenarios. The location of the current pulse is shown using dashed line. Figures 21(a) and 21(b) show that the histogram comparison method accurately detects heating in the top die resistor, even in the presence of background thermal activity. The

SSIM index method shows much greater noise, which may be an additional disadvantage. It is also interesting to note that the degree of similarity predicted by the SSIM index method decays very slowly following the end of the heating pulse, whereas the histogram method returns to the baseline level quite rapidly. Since there is more heat generated in active circuit case, the average temperature rise in Figure 21 (b) is slightly higher than in Figure 21(a). Note that Figure 21 captures the thermal interactions between the two die in the stack, which is unique to the 3D IC architecture.

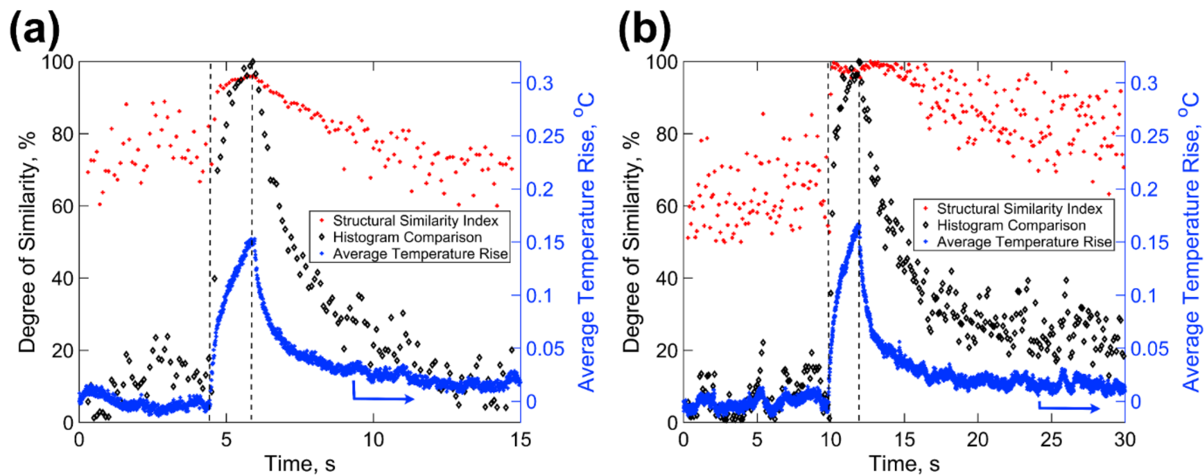

Figure 21 – Measured average temperature rise and degree of similarity plotted as functions of time for 5 mA pulsed heating current through the top die resistor. Data are shown for SSIM index and histogram comparison methods. (a) shows data without background heating, and (b) shows data with background heating produced by 10 mA heating current through the bottom die resistor.

In order to demonstrate that additional data filtering can further facilitate Trojan detection, thermal noise reduction is carried out on the data shown in Figure 21(b). Figure 22 presents these data in binary format, which helps understands the importance of thermal noise reduction. Figure 22(a) shows the thermal map before the heating current is passed, whereas Figure 22(b) shows the thermal map at 2.1 s after both top die and bottom die resistors are heated with 10 mA current. The use of a median filter for noise reduction is demonstrated in Figure 22(c). The median filter is a

commonly used image processing tool which reduces 'salt and pepper' noise [77], such as the thermal noise observed in Figure 22(b). The median filter replaces each pixel with the median value of a 3×3 matrix surrounding the pixel. As shown in Figure 22(c), this significantly helps in noise reduction, thereby making it easier to detect unusual thermal activities. Specifically, with the use of median filter, the occurrence of false negatives that may be caused by thermal noise shown in Figure 22(b) can be reduced significantly.

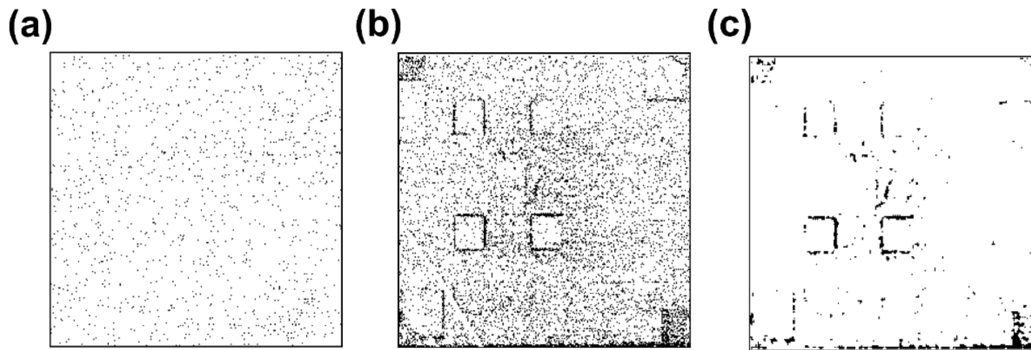

Figure 22 – Temperature maps after thermal noise reduction for the case of 5 mA heating pulse through the top die resistor, with background heating produced by 10 mA heating current through the bottom die resistor. (a) shows baseline state before the onset of current; (b) shows state 2.1 s after the onset of current; (c) shows state after the onset of current, with the application of median filter.

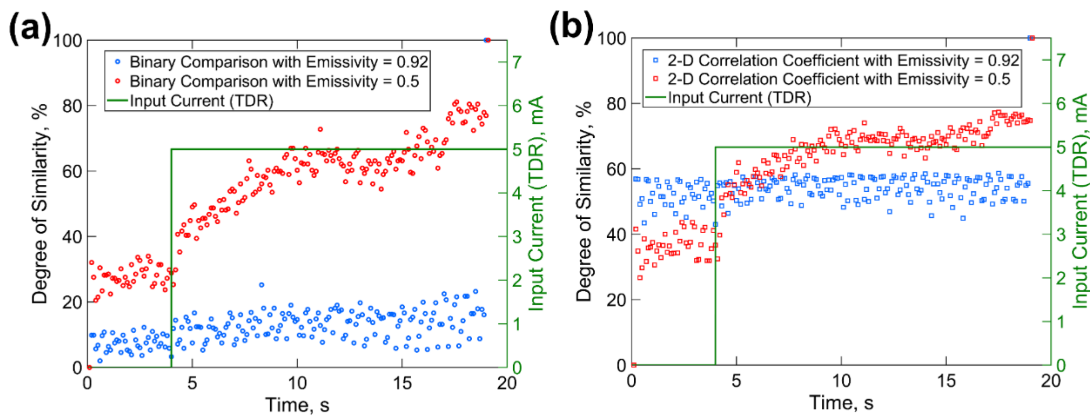

Figure 23 – Effect of change in the value of emissivity used in infrared thermography. (a) and (b) show the degree of similarity as a function of time for the case of 5 mA heating current through the top die resistor. Data are shown for (a) binary comparison method, and (b) 2D correlation coefficient method.

Finally, it is shown that the poor performance of binary comparison and 2D correlation coefficient methods at small current inputs can be improved by changing the emissivity value used to acquire temperature data from infrared images in ResearchIR software. Figure 23(a) and (b) plot the degree of similarity as a function of time for 5 mA heating current through the top die resistor predicted by these two methods. In each case, plots with emissivity values of 0.92 and 0.50 are both shown. Figures 23(a) and 23(b) show that lowering the emissivity significantly improves the performance of both methods. The degree of similarity remains flat despite the heating signal when the emissivity is 0.92, but there is a greater deviation when using a lower value of emissivity. Even though changing the emissivity value may result in inaccurate prediction of temperature, that may not be important, since the goal here is to detect a thermal activity rather than accurately measure the temperature. It is interesting to note that there is little effect of emissivity on the accuracy of SSIM index or histogram comparison methods.

3.4.4. Validity of backside infrared imaging

A key component of this work is the imaging of the chip from the backside in order to optically access the transistor plane. Backside imaging is more practical than frontside imaging, since the frontside is usually occupied by electrical interconnection, as is the case in the chip used in this work. IR imaging of the backside of the chip still allows measurement of temperature field on the transistor plane because of the IR-transparent nature of Silicon [63]. In order to independently confirm this, a separate experiment is carried out on a single-die Silicon chip comprising MOSCap circuits fabricated on the frontside. A thin graphite film is sprayed on the backside of one half of the chip, while the other half is left bare. The chip is placed upside down on a hot plate maintained at 50 °C. Figure 24(a) shows a regular picture of the chip, whereas Figure 24(b) shows an infrared image. Chip orientation is the same in both images. As shown in Figure

24(a), the top half of the chip is sprayed with graphite. IR imaging of the corresponding region is quite uniform, whereas, IR imaging of the bottom half of the chip that is not sprayed with graphite reveals circuit features from the frontside. This shows that backside infrared imaging – without graphite coating – is able to access the transistor plane of the chip due to the infrared-transparent nature of Silicon. This feature is a key enabler for IR-based Trojan detection because in most cases, only the backside of the chip is available for imaging. Note that the absolute temperature measured here is not as critical as the ability to detect frontside features, leading to detection of Trojan activity.

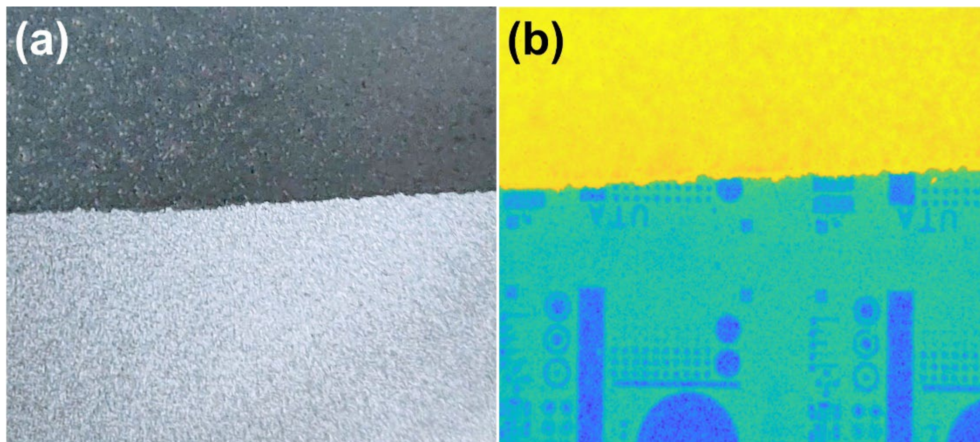

Figure 24 – Demonstration of the impact of graphite layer on the backside of a MOSCap imprinted Silicon die. Graphite is sprayed on the top half of the die. (a) and (b) show white light and infrared images of the die backside, respectively, when the chip is placed upside down on a hot plate maintained at 50 °C.

Chapter 4

Experimental and Theoretical Analysis of Immersion Cooling of a 21700 Li-Ion Battery Module and its Impact on Accelerated Cell Aging

Submitted as: Swapnil S. Salvi[1], Bapiraju Surampudi[2], Andre Swarts[2], Jayant Sarlashkar[2], Ian Smith[2], Terry Alger[2], Ankur Jain[1,*] (2022). Experimental and Theoretical Analysis of Immersion Cooling of a 21700 Li-Ion Battery Module and its Impact on Accelerated Cell Aging.

4-1. Introduction

Li-ion batteries play a key role in energy storage and conversion in electric vehicles (EVs) and several other engineering systems. Improving the energy density and discharge rates in battery packs is of critical importance for maximizing the performance and driving range of EVs. A key technical challenge here is the strong temperature sensitivity of Li-ion cells, including rapid performance degradation at both low and high temperatures [78,79]. Moreover, serious safety concerns related to thermal runaway and fire occur when the battery temperature exceeds a certain threshold [80]. Therefore, a well-designed thermal management system for the automotive battery pack is critical [81]. Since experimental measurements may often be time-consuming and expensive, development of robust theoretical models and numerical simulations is essential for scientific understanding and engineering optimization [82].

A vast amount of past work on modeling and simulations for battery thermal management is already available, for both steady state [83] and transient [84] conditions. A conjugate analytical model for flow cooling of a battery pack has been proposed [85]. Thermal resistance network-based modeling has been carried out to predict the performance of an air-cooling system coupled with a micro heat pipe array for cooling a prismatic battery pack [86]. Multiscale multidomain modeling has been carried out for a liquid-cooled Li-ion battery pack of 24 prismatic cells, which claims to maintain the peak temperature in the battery pack under 40 °C and maximum temperature difference across the whole battery pack around 5 °C even at a discharge rate of 5C [87]. Another study using COMSOL Multiphysics has been carried out to compare forced air convection, heat pipe and heat pipe with copper sheets, for which, an improvement in temperature uniformity of 39%, 67% and 73%, respectively, has been reported [88]. Analytical models have also been used to predict the internal temperature of a Li-ion cell, which is an important parameter that is difficult to measure directly [89–92]. A few thermal simulation models that account for the dynamics of

electrochemical heat generation have also been reported [13–15]. Several studies have modeled thermal effects using resistance network techniques [96–102]. The sub-modeling technique has been used for resolving the large variation in length scales in thermal simulation of a large battery pack comprising thousands of cells [103].

Key battery thermal management techniques include cooling based on air [104,105], liquid [106,107], heat pipe [108,109], thermoelectric [110,111] and phase change materials [112,113]. Hybrid approaches that combine multiple techniques have also been reported [114–116]. Among these techniques, immersed liquid cooling offers very high efficiency due to high heat capacity and heat transfer coefficient, reduced equipment cost, and lower thermal expansion compared to PCMs [112]. Unlike cooling by liquid flow in serpentine tubes between cells, immersion cooling enables direct cell-coolant contact, leading to greater heat dissipation, and thus reduced thermal runaway propagation [117,118]. Experimental investigation of immersion liquid cooling for a battery pack and comparison with thermal management system based on serpentine tubes between rows of cells has been presented previously [117]. In another work, a 47% reduction in battery pack peak temperature at 3C discharge rate was reported for immersion cooling with a dielectric fluid compared to natural convective cooling [118]. A study of preheating of the battery pack in cold ambient using a hot fluid flowing around the battery in an immersed arrangement has been reported. It was found that preheating resulted in very good temperature uniformity, within 4 °C throughout the battery pack [119]. A numerical study of fast-charging of a Li-ion battery pack based on direct immersion cooling using hydrofluoroether coolant showed improved mass energy density and lower coolant pump power consumption [120]. Despite the clear benefits of immersion cooling, however, there remains a lack of work that investigates the impact of immersion cooling on electrochemical performance of the battery pack. Such concerns may arise, for example, due to

prolonged exposure to the dielectric fluid and the possibility of non-uniform cooling of cells during immersion cooling.

This paper presents experimental and simulations-based investigation of the thermal and electrochemical impact of immersion cooling during fast charging of a Lithium-ion cell module. The module is subjected to a fast charge duty cycle comprising fast charge profiles interspersed with rest periods and nominal discharge for up to five weeks. A Reference Performance Test (RPT) is carried out each week to characterize aging effects by measuring discharge capacity fade, power fade and resistance growth. Electrochemical Impedance Spectroscopy (EIS) measurements are carried out to identify possible lithium plating effects. Analytical and numerical simulation models are developed to identify the dominant thermal and electrochemical effects of immersion cooling. A comparison between measurements and models is carried out in order to help understand the impact of immersion cooling on cell aging, and possible underlying mechanisms.

The rest of this paper is organized as follows: Section 2 describes the experimental setup and measurements carried out in this work. Section 3 presents a theoretical heat transfer model and simulations carried out to model the system-level thermal dynamics during immersion cooling and to estimate cell internal temperature. Key results are discussed in Section 4, followed by conclusions in Section 5.

4-2. Experimental apparatus

Despite the significant potential for effective cooling of Li-ion cells using immersion coolants, particularly for Li-ion cells, there are no standards available for evaluating the performance of immersion coolants. This section describes an experimental test bed for

investigating the immersion cooling of a battery pack. Key experimental details, including cells, coolants, measurement setup and process are described below.

4.2.1 Experimental setup

A seven-cell module shown in Figure 25(a) is constructed using LG Chem M50T 21700 cylindrical cells with lithium nickel manganese cobalt oxide (NCM) cathode and graphitic anode. The nominal cell capacity and impedance are 18.2 Wh and 30 mΩ, respectively. As shown in Figure 25(a), the cells are interconnected in a 7PS1 configuration using spot welding on nickel metal bus bars to form a flower-shaped cross section. The cell-to-cell gap is approximately 0.5 mm. Omega K-type thermocouples are glued using thermal paste and taped on the cylindrical surface of each cell. The SBT-2050 Power Cycler from PEC Corp is used for implementing a fast charge current profile. Data acquisition from all thermocouples is carried out using an NI Compact-RIO based data acquisition system.

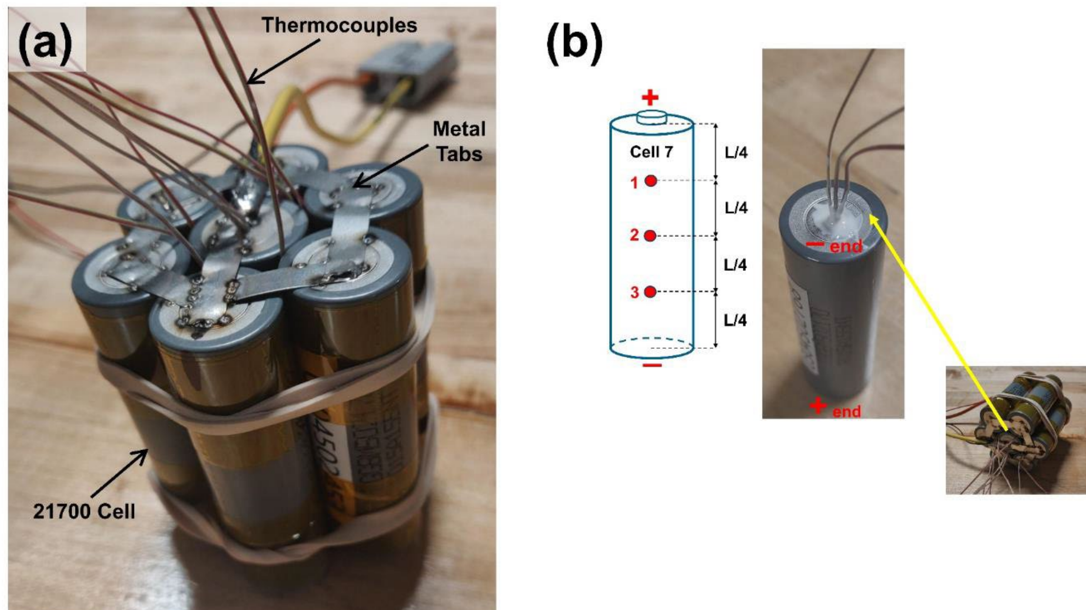

Figure 25. Pictures of experimental setup for immersion cooling of a seven-cell battery pack: (a) Module of seven 21700 cells tabbed together in 7PS1 arrangement, (b) Central cell instrumented with thermocouples in the core at locations as shown.

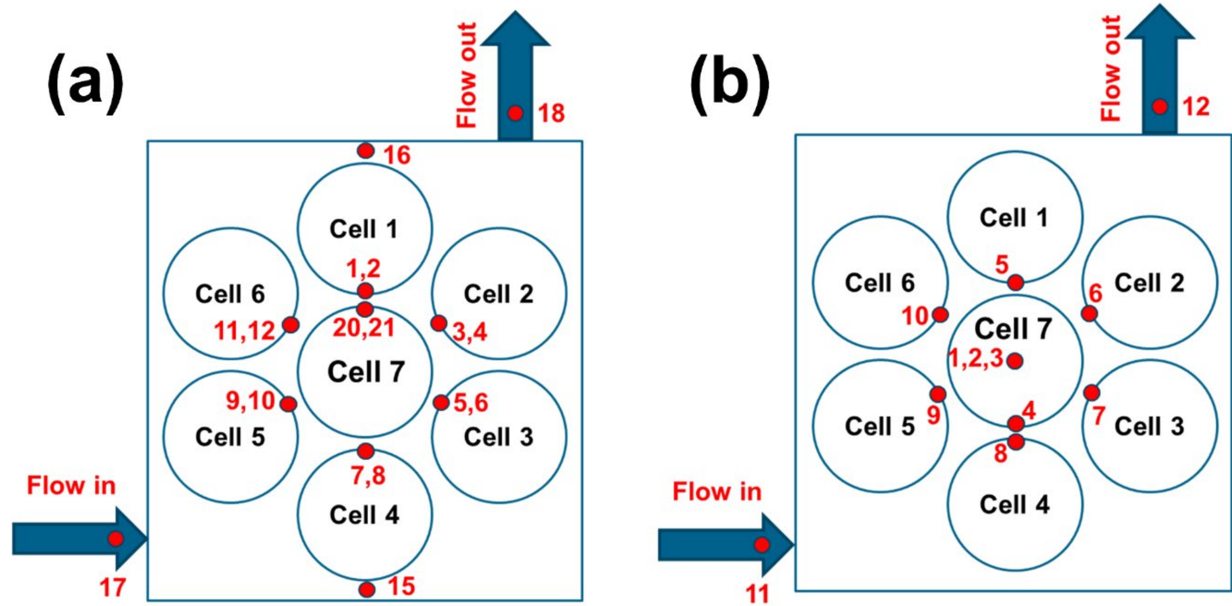

Figure 26. Thermocouple locations for (a) surface and (b) core temperature measurement (thermocouples 1-3 as shown). The schematics are drawn as viewed from the positive terminal end of the cells.

In addition, for experiments involving internal temperature measurements, the central cell in the flower configuration of 7PS1 module is drilled axially from the negative tap side (Figure 25(b)). The drill bit is handled carefully to avoid damage to the jelly roll inside the cell. Once the thermocouples are inserted inside the cell, the opening is quickly sealed with marine epoxy [121,122]. The locations of thermocouples for testing during baseline and immersion cooling cases are shown in Figure 26(a). For the experiment with internal temperature monitoring, thermocouples are also placed in the core cavity of cell's jelly roll as indicated by locations 1, 2 and 3 in Figure 25(b) and Figure 26(b).

Figure 27 presents pictures of the overall experimental set up and the specific test rig that houses the battery pack. Figure 28 shows a schematic of the fluid flow circuit and related instrumentation. The module is positioned centrally in test rig, which is customized to allow coolant flow around the cells. The test rig is large enough to accommodate the module with a clearance of around 5 mm between cells and test rig walls. This avoids direct electrical contact and

offers sufficient space for essential wirings from module to the cell cycler and thermocouples. At a flowrate of 1.5 liters per minute (LPM), the liquid sweeps out the entire coolant volume in the test rig every 10-20 seconds. The test rig is designed with only 38% excess fluid volume compared to the volume of seven cells, resulting in a compact configuration with minimum add-on weight to remain conducive for practical applications. Coolant flowrate and temperature are controlled using a flow control valve and a 3-way mixer valve respectively, as shown in Figure 28. The mixer valve mixes cold fluid from a heat exchanger leg and a hot fluid from heater leg to achieve the target temperature. As shown in Figure 29, the fluid inlet and outlet are on one of the side faces and the top face, respectively. Both are instrumented with thermocouples to measure inlet and outlet coolant temperatures. In addition to baseline measurements without any immersion cooling, fast charge aging tests are also conducted for two different coolant liquids – Novec 7000, a well-known dielectric fluid [123] and a test liquid referred to as 'Fluid X'. Thermal transport properties of the two coolants are listed in Table 4.

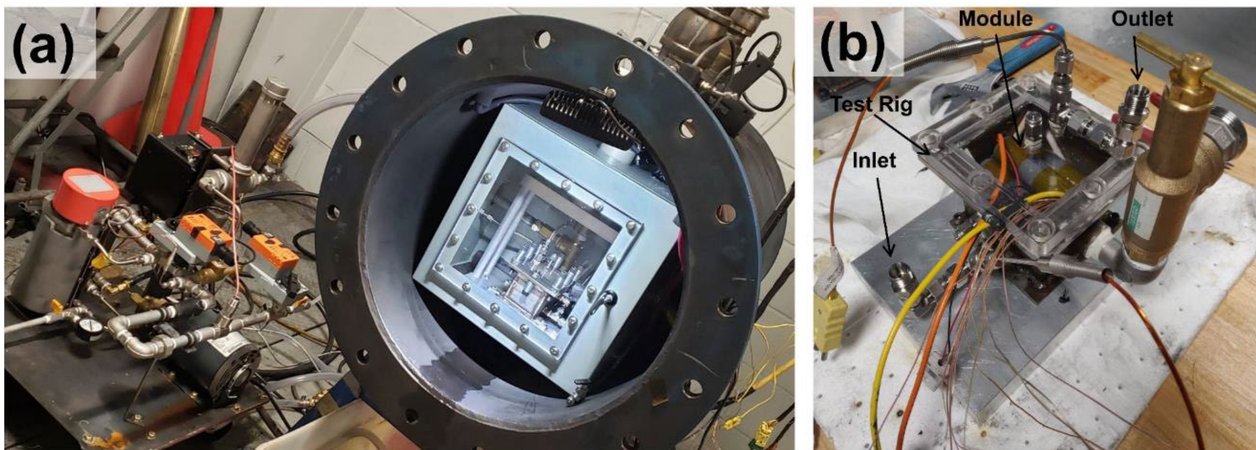

Figure 27. (a) Test enclosure with coolant setup, (b) instrumented test rig along with the module.

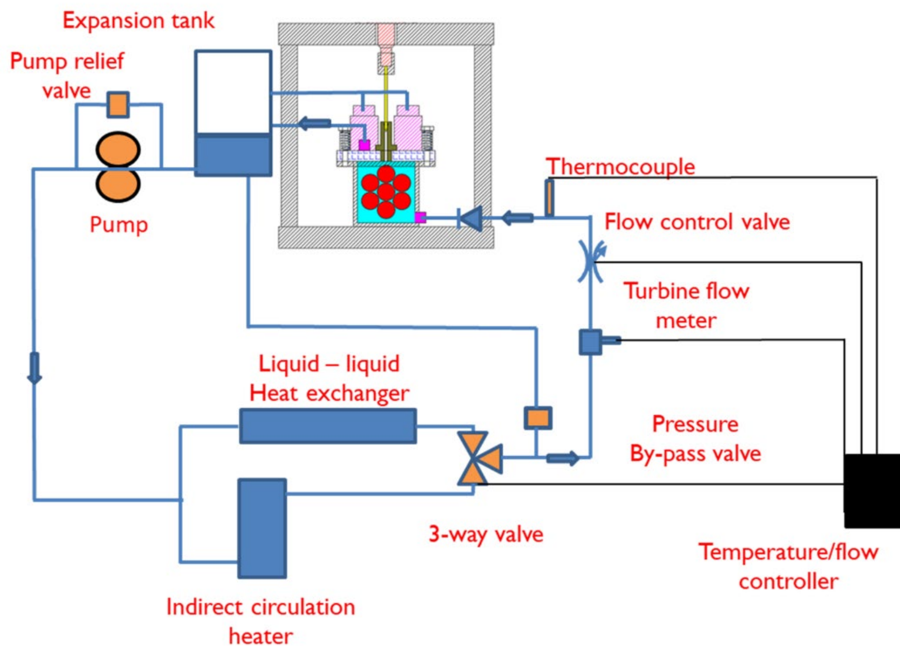

Figure 28. Schematic of the test setup showing the fluid flow circuit and associated instrumentation.

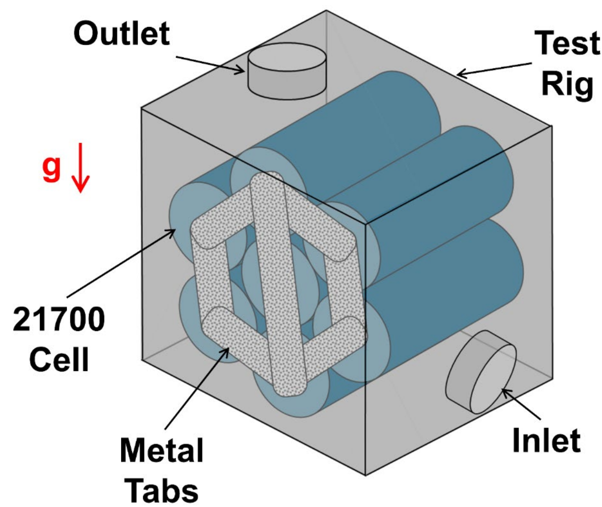

Figure 29. Schematic showing the experimental setup for immersion cooling of seven-cell battery pack.

Table 4 Thermal properties of the immersion coolant fluids used in this work

	Boiling Temperature (°C)	Thermal Conductivity ($Wm^{-1}K^{-1}$)	Latent heat of vaporization ($kJkg^{-1}$)	Specific Heat ($kJkg^{-1}K^{-1}$)
Fluid X	330	0.143	-	2.1
Novec 7000	34	0.075	142	1.3

4.2.2 Experimental procedure

Measurements are carried out with two key goals – to evaluate cell performance and capacity fade due to multi-week cycle aging, and to monitor the internal temperature of the cell for a few cycles carried out in a 24-hour period. Performance with immersion cooling using either Novec7000 or Fluid X at 1.5 LPM flowrate and 25 °C inlet temperature is compared with the baseline case with no immersion cooling.

As shown in Figure 30, the module undergoes charge-discharge cycling for five days, followed by a Reference Performance Test (RPT) on the fifth and sixth days. Charge-discharge cycling comprises one hour of rest period, followed by constant current constant voltage (CCCV) charging at 0.7C, which is the maximum continuous current specification, then one hour rest and finally constant current (CC) discharge at 0.2C, corresponding to the nominal current. The cells are cycled between 4.2 V and 2.5 V.

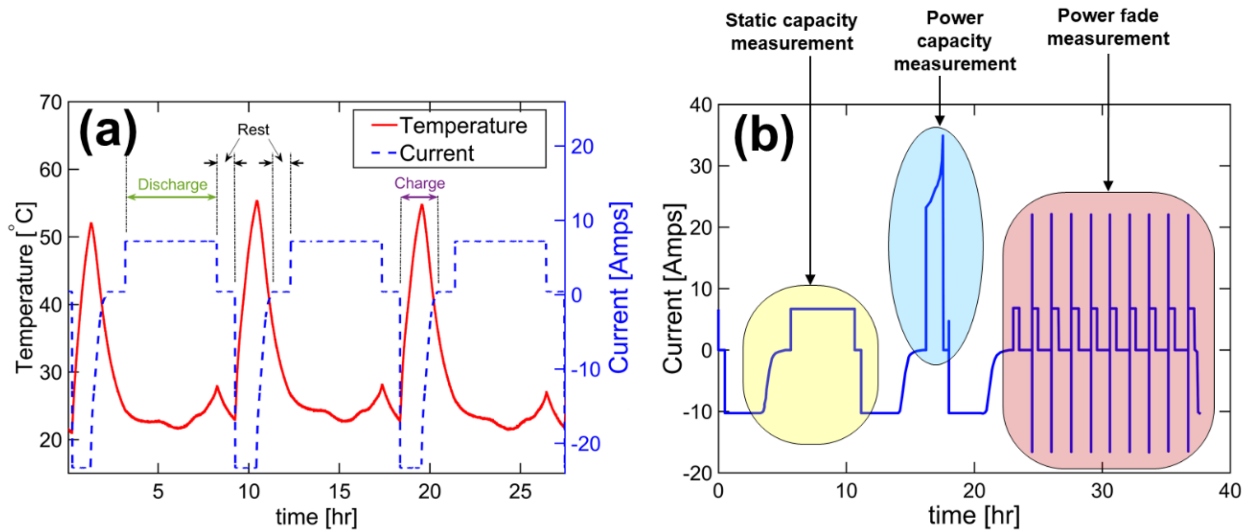

Figure 30. (a) Typical current profile used for testing. The corresponding temperature curve is also shown. (b) A typical Reference Performance Test (RPT) profile.

Electrochemical Impedance Spectroscopy (EIS) is a non-invasive frequency response technique to highlight patterns of lithium plating in the cell or module. A Gamry 1010 EIS analyzer is used to stimulate the cell with sinusoidal currents of amplitude 20 mA with frequencies from 0.1 Hz to 5 kHz. The resulting frequency response Nyquist plot in the complex domain helps understand the lithium plating process and other internal cell dynamics [124]. For example, Figure 31 shows a typical Nyquist plot showing different frequency regimes that may be used to understand different transport processes that occur within the cell. Specifically, the minima noted in Figure 31 provides information about the nature of Lithium plating in the cell. Since this method is ex-situ, an impulse response based pseudo-EIS procedure [125] is also carried out. This procedure can be carried out real time or in-situ during life testing or in an actual BMS in a vehicle or grid storage. The real impedance value is extracted from both types of EIS tests and may be plotted as a function of SOC. These electrochemical measurements help understand the dynamics of lithium plating that may occur in the cell, especially at large C-rates.

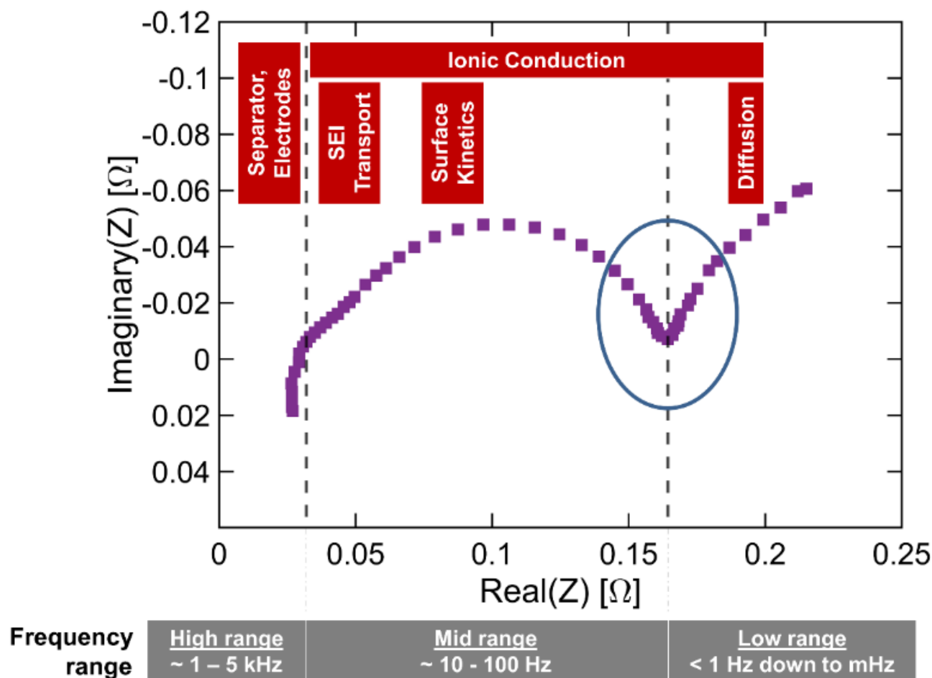

Figure 31. A representative Nyquist plot from EIS measurements, with the minima associated with lithium plate phenomenon shown [124].

4-3. Theoretical modeling

Theoretical and simulations-based analysis is carried out for an improved understanding and interpretation of experimental data, particularly towards understanding the impact of immersion cooling on cell aging. For the immersion cooling method, radiative heat dissipation is likely to be negligible due to continuous flow of a dense liquid, such as the ones used here, around the cells. This analysis first focuses on showing that radiation effects are negligible and investigating the likelihood of large temperature differentials between the core and surface of the cell. For the baseline case, the module is assumed to be surrounded by stagnant air at room temperature, with heat transfer occurring due to natural convection alone. In contrast, in cases where immersion coolant due to liquid flow around the module occurs, the dominant heat transfer is assumed to be forced convection. The central cell of the module experiences the most severe cooling conditions compared to other cells on the periphery of the module. Measured surface temperatures of all the seven cells in the module support this assumption. Hence, the thermal behavior of only the central cell is analyzed for simplicity. Finally, analysis carried out in this paper focuses only on the charging region, due to much higher temperatures observed during fast charging than the rest of the cycle.

4.3.1 Analytical modeling

In this sub-section, analytical modeling for the baseline case as well as immersion cooling case is described.

4.3.1.1 Surface temperature of the cell

A thermal resistance network based analysis is carried out in order to estimate the surface and core temperatures of each cell, as shown in Figure 32. Radiation is considered only for the baseline case. Energy balance equation for an individual cell can be defined as follows:

$$mC_P \frac{dT}{dt} = Q_{Gen} - Q_{Conv} - Q_{Rad} \tag{1}$$

where $Q_{Conv} = (T_{Cell} - T_f)/R_{Conv}$ and $Q_{Rad} = (T_{Cell} - T_f)/R_{Rad}$ are the convective and radiative heat losses. $R_{Conv} = 1/(hA)$ and $R_{Rad} = 1/(A_{Cell}\varepsilon\sigma(T_f+T_{Cell})(T_f^2+T_{Cell}^2))$ are the convective and radiative thermal resistances. Numerical values of various parameters used here are summarized in Table 5.

On the other hand, heat generation rate for a single cell can be calculated by [126]:

$$Q_{Gen} = I(U_{OC} - V) + I\left[T_{Cell}\frac{dU_{OC}}{dT_{Cell}}\right] = I^2R_e + I\left[T_{Cell}\frac{dU_{OC}}{dT_{Cell}}\right] \tag{2}$$

The first term in equation (2) represents irreversible heat whereas the second term shows the reversible entropic heat. Finally, from eqs. (1) and (2), a detailed energy balance equation for an individual cell can be derived:

$$m_{Cell}C_{P_{Cell}}\frac{dT_{Cell}}{dt} = I^2R_e + I\left[T_{Cell}\frac{dU_{OC}}{dT_{Cell}}\right] - \left[\frac{T_{Cell} - T_f}{R_{Conv}}\right] - \left[\frac{T_{Cell} - T_f}{R_{Rad}}\right] \tag{3}$$

The gradient of open circuit voltage as a function of cell temperature is calculated from experimental plots of open circuit voltage as a function of the state of charge and then relating state of charge with cell temperature.

4.3.1.2 Surface and core temperature of the cell

As shown in Figure 32, the thermal resistance network in this problem comprises a convective and a conductive resistance in series between the fluid, cell surface and cell core temperatures, with heat generation being supplied to the cell temperature nodes. The outcome of previous model explained in 4.3.1.1 conveys that the radiation must be ignored – this has been justified in Section 3 and is discussed in more detail in Section 4. Detailed energy balance for an individual cell considering both the surface as well as core temperatures can be written as a set of two coupled differential equations which can be solved simultaneously:

$$m_{Core} C_{P_{Core}} \frac{dT_{Core}}{dt} = I^2 R_e + I \left[T_{Core} \frac{dU_{OC}}{dT_{Core}} \right] - \left[\frac{T_{Core} - T_{Surf}}{R_{Cond}} \right] \tag{4}$$

$$m_{Surf} C_{P_{Surf}} \frac{dT_{Surf}}{dt} = \left[\frac{T_{Core} - T_{Surf}}{R_{Cond}} \right] - \left[\frac{T_{Surf} - T_f}{R_{Conv}} \right] \tag{5}$$

Where, C_{PCore} [127] and C_{PSurf} are heat capacities of jelly roll and metal shell, respectively, and T_{Core} and T_{Surf} are cell surface and core temperatures, respectively. Finally, R_{Cond} is the conductive thermal resistance of the jelly roll, taken from the literature to be 3.3 KW^{-1} [128]. Numerical values of these parameters are listed in Table 5.

Equations (3)-(5) are numerically solved using Simulink software, in order to determine T_{Cell}, T_{Surf} and T_{Core} as functions of time.

Table 5. Numerical values of various parameters used in the simulation model

Parameter	Numerical Value
C_P	715 $Jkg^{-1}K^{-1}$ [50]
σ	5.67×10^{-8} $Wm^{-2}K^{-4}$
M	0.068 kg
m_{core}	0.06 kg
m_{Surf}	0.008 kg

4.3.2 Simulink modeling

Equations (3), (4) and (5) are ordinary differential equations (ODEs) that govern the cell temperature distribution as a function of time. These equations are converted to a block diagram in the Simulink workspace using integrator, algebraic and functional blocks from various libraries. ODE45 solver is used for numerical integration of the ODEs. Temperature, heat estimates and other state data are collected into the workspace for post-processing.

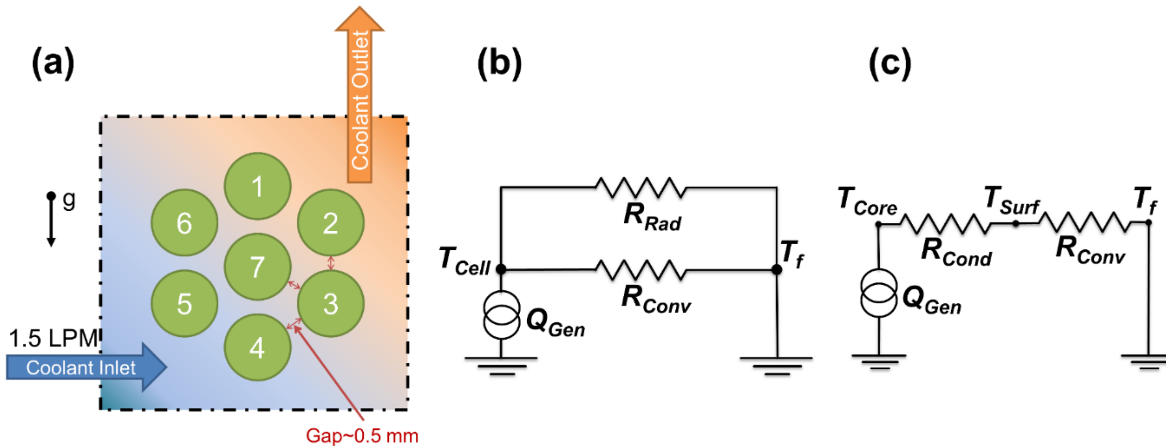

Figure 32. (a) Schematic description for problem definition, (b) Thermal resistance network (considering effective radiation), (c) Thermal resistance network (considering core temperature along with cell surface temperature).

4.3.3 Numerical modeling

A finite volume model is developed in ANSYS Fluent in order to visualize the nature of fluid flow in the experimental setup. The geometry of the experimental setup is created in ANSYS SpaceClaim. Enclosure and battery module are modeled according to the description in section 2.1. Suitable fluid domains are created to simulate fluid flow around the cells inside the enclosure. Grid independence is verified, resulting in a mesh comprising around 1.5 million nodes and 9 million elements. Only the momentum equations are solved in these simulations, since the focus is to visualize the flow fields to verify and support the assumptions used in analytical modeling.

Values of convective heat transfer coefficients are obtained from these simulations, for use in Simulink models described in section 4.3.2.

4-4. Results and Discussion

4.4.1 Hypotheses for Capacity Fade

Figure 33 plots the measured percentage discharge capacity fade as a function of the number of RPTs, where an RPT is carried out at the end of every week of cycling. Each RPT in Figure 33 represents roughly one week of calendar time and 20 fast charge cycles. It can be observed that after four RPTs, the total capacity fade for Fluid X immersion cooling case is around 5%, compared to 4.2% for the baseline case. The more rapid deterioration of battery capacity in the case of immersion cooling may be somewhat counter-intuitive. Based on aging data on these cells at various temperatures measured in the past, Figure 34 shows that an average rise of temperature of 2 ºC for the Fluid X immersion cooled cells is needed to explain the increased capacity fade.

The following hypotheses are tested as possible explanations for this phenomenon:

1. (Hypothesis A) Reduced radiation heat transfer due to lower emissivity due to fluid occlusion: It has been reported [129] that certain coatings on cylindrical cells may result in high surface emissivity and thus enhanced radiation heat transfer. This may result in faster heat dissipation in the baseline case compared to the immersion cooling case.

2. (Hypothesis B) Greater non-linear heat transfer gradient inside the jelly roll due to aggressive surface cooling: It has been shown [130,131] that a non-uniform thermal gradient developed inside the cell directly affects the performance and eventually deteriorates the life of the cell. The temperature gradient may result in simply a higher core temperature or an intermediate

maximum inside the jelly roll if the core temperature is not significantly high. Using estimates of convective heat transfer coefficient for the baseline and immersion cooling cases in the present work, the value of the Biot number for these cases are estimated to be around 0.02 and 0.57, respectively. This indicates that there may be a temperature maximum inside the jelly rollin the immersion cooling case. Further, analytical modeling of surface-cooled and tab-cooled Li-ion battery arrangement [130,131] has shown that the tab-cooled cell has better performance despite greater operational temperature, compared to a surface-cooled cell, which has a much more non-homogeneous temperature distribution. This finding provides a justification to consider this hypothesis.

3. (Hypothesis C) It is well-known that Li-ion cells exhibit lithium plating at low temperature and high charge rate [79]. The aggressive cooling in the immersion cooling case may result in the surface temperature being close to ambient even while the battery is being fast charged. This may result in further lithium plating and higher capacity fade. EIS measurements are carried out to explore this hypothesis further.

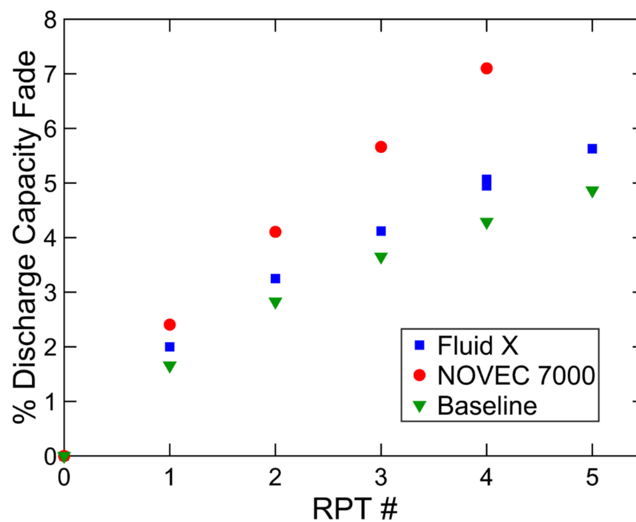

Figure 33. Capacity fade as a function of number of RPTs (reference performance tests). Data are shown for baseline (no cooling) as well as cooling with two different coolant fluids.

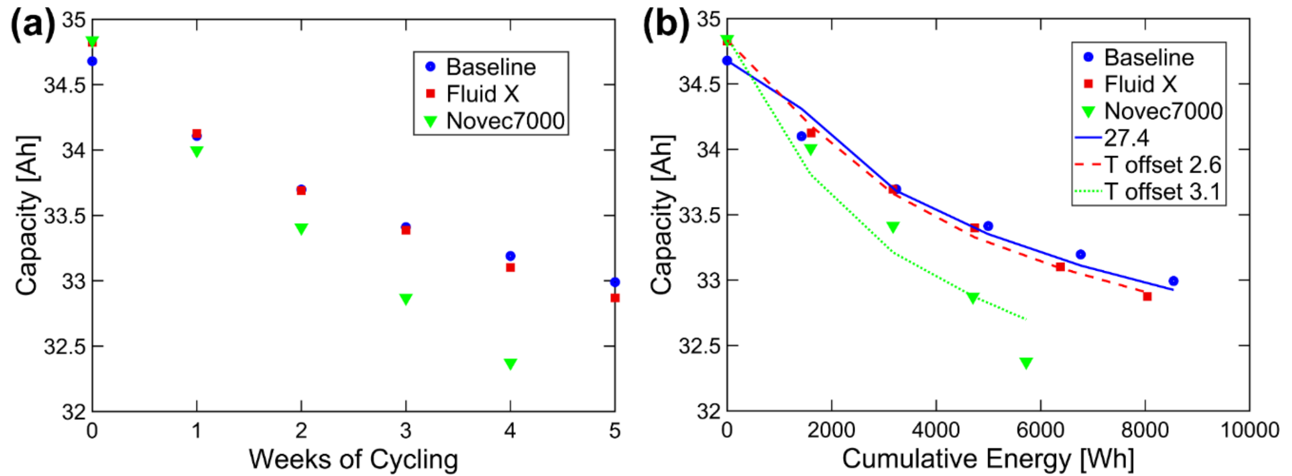

Figure 34. (a) Actual capacity fade and (b) Modeled capacity fade assuming average temperature offsets due to gradients to explain aging.

4.4.2 Baseline Case Results Discussion

For baseline case experiments, the surrounding medium is stagnant air and thus the dominant heat transfer mechanism is natural convection around the cells, with convective heat transfer coefficient h varying as a function of air temperature [132,133]. To explore Hypothesis A discussed in the previous section, a radiative heat transfer term is considered. A suitable value for emissivity of the outer cell surface, $\varepsilon = 0.7$ [129] is used. Surface temperature of the cell can be calculated by solving eq. (3) in Simulink, initially considering the effect of radiative heat transfer. Referring to Figure 35(a), a transient thermal distribution for surface temperature of cell over multiple charge-discharge cycles shows that the theoretical model that includes radiation does not match well with the experimental results. Due to consideration of radiative heat dissipation along with convective heat dissipation, the surface temperature is underestimated. On the other hand, referring to Figure 35(b), without consideration of radiative heat dissipation, i.e., $\varepsilon = 0$, there is much better agreement, with rise in surface temperature of approximately 25 °C. This shows that radiation is not likely to be a dominant heat transfer mechanism in the immersion cooling conditions considered here. Based on this analysis, Hypothesis A is ruled out.

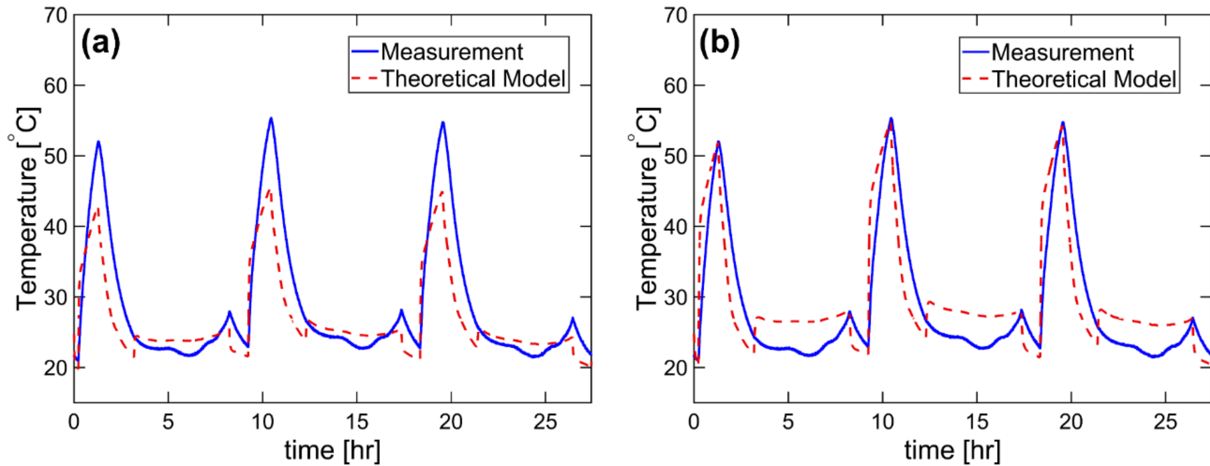

Figure 35. (a) Temperature vs time for baseline case (Surface temperature model) considering (a) convective as well as radiative heat dissipation, (b) only convective heat dissipation.

4.4.3 Fluid-X Immersion Cooled Case Results Discussion

A comparison of experimental measurements of immersion cooling case and the analytical model based on eq. (3) presented in Figure 36 shows very good agreement between the two. Due to aggressive forced convective cooling, the surface temperature of the cell rises only by 1-2 °C, compared to 30 ºC rise for the baseline case. Only convective heat transfer terms are considered in the model. From the ANSYS Fluent model, which considered the mixed (annular and peripheral) flow effects and previous literature [132,134], a value of h = 90 $Wm^{-2}K^{-1}$ is extracted for the lumped convective heat transfer coefficient) for use in the Simulink model above.

For a set of parameter values consistent with experimental conditions, visualization of the flow field from the Fluent model is shown in Figure 37. The flow fields are as anticipated and low flow resistance regions are clearly delineated. There is no significant flow between the cells, indicating that the center cell has the least direct exposure to fluid. This also shows that location of the ports can cause significant stagnant regions, leading to asymmetric cell cooling in larger battery packs. It can be observed that the flow field is a combination of annular as well as circumferential flow, i.e., an axial flow along the cell length and a radial flow around the cell

radius, respectively. The 0.5 mm gap among the cells offers a much greater flow resistance compared to the 5 mm gap between cells and enclosure walls, which, in turn, promotes annular flow even if the inlet and outlet are designed to achieve circumferential flow. These results support the assumption related to convective heat transfer coefficient to be around 90 W/m^{2}K.

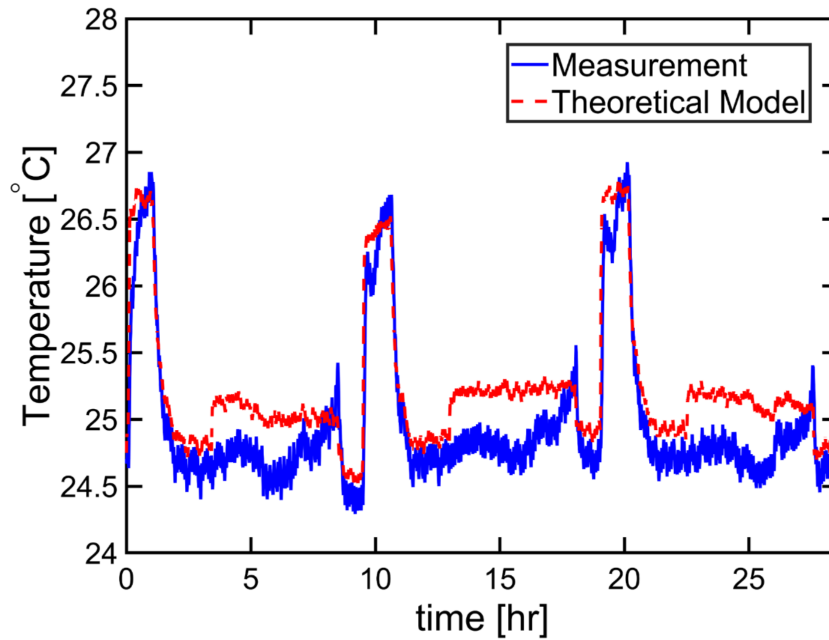

Figure 36. Temperature vs time for Fluid X case (Surface temperature model) considering only convective heat dissipation.

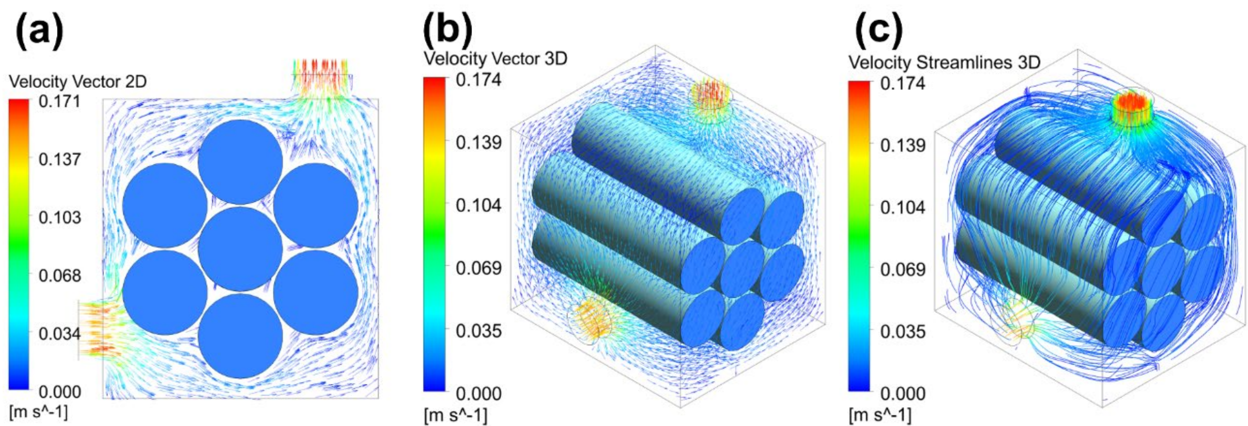

Figure 37. Finite-element simulation results for a set of parameter values consistent with experimental conditions: (a) 2D Velocity vectors (top view), (b) 3D Velocity vectors, (c) Velocity streamlines.

4.4.4 Cell Core Temperature Measurement Discussion

Internal temperature measurements are carried out in one of the cells in the immersed module to understand whether the core temperatures become too high during aggressive surface cooling. The goal of this experiment and analysis is mainly to explore Hypothesis B presented in the previous section. Eqs. (4) and (5) are solved simultaneously using Simulink to calculate the surface and core temperature of the cell, respectively. A comparison of measured and theoretically predicted internal and surface temperature is shown in Figure 38 and 39 for baseline and immersion coolant cases, respectively. In both cases, there is good agreement for surface and core temperatures in the fast-charging region. The value of a thermal conductive resistance – R_{Cond} – is based on previously reported experimental studies [128], which matched core temperature measurements with an analytical model to extract this parameter. The temperature difference between core and surface temperatures of the cell in both the cases is found to be around 1 ℃, which eliminates the possibility of a higher temperature difference from the core to surface in case of immersion cooling method using Fluid X. As a direct result of this observation, Hypothesis B is ruled out. It is important to note, however, that this does not fully preclude the possibility of higher temperatures in the middle of jelly roll with low temperatures at the core and surface.

To further understand other possible unobservable internal states, a sensitivity analysis is carried out to understand the sensitivity of the temperature gradient to varying properties such as internal conductivity, convection heat transfer coefficient and charge current. Results are presented in Figure 40. It can be observed that while the core-surface temperature difference is directly influenced by the conduction resistance, it is largely insensitive to the value of the convective heat transfer coefficient. However, smaller values of convective heat transfer slow down the rate of transient rise of the temperature difference, thus increasing the average temperature of the jelly roll. Charging current also has a prominent effect on the core-surface temperature difference, since

the heat generation in the cell directly depends on current. When interpreted in the context of fast charge rates for immersed battery packs, this result indicates that without proper thermal management, increasing charge current is detrimental to life due to higher internal temperatures. A key takeaway from the sensitivity analysis is related to distribution of internal thermal conductivity of the jelly roll. The jelly roll can be considered as layers of cells in series and as such the thermal conductivity of each layer can change with internal temperature distribution and resistance inhomogeneity. If the thermal conductivity is thus lower in the middle of the jelly roll compared to the outer layers, this may lead to excessive internal temperature peak. Unfortunately, a direct measurement is difficult since sensors are not usually embedded inside the jelly roll during manufacturing. The Tesla-Panasonic 4680 cell design with dedicated tabs for inner layers is a testament to the need to dissipate this inner heat more effectively.

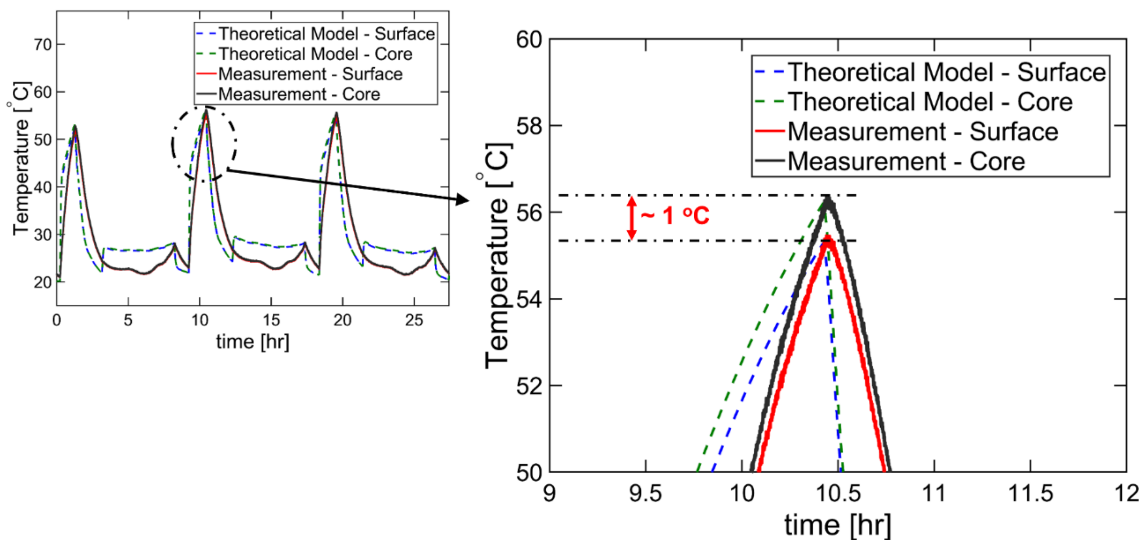

Figure 38. Temperature vs time for Baseline case (Core and surface temperature model) – focusing on difference between core and surface temperatures and comparison with experimental core and surface temperature.

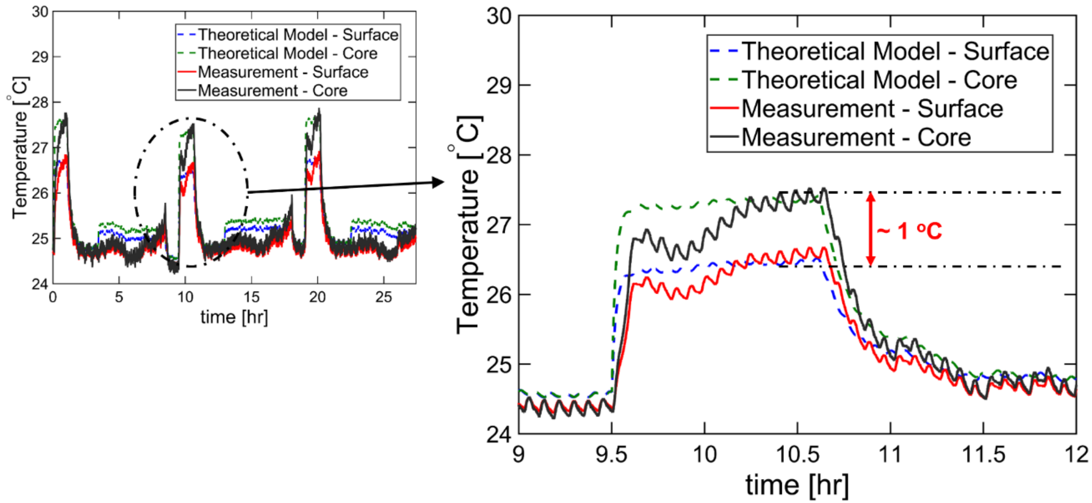

Figure 39. Temperature vs time for Fluid X case (Core and surface temperature model) – focusing on difference between core and surface temperatures and comparison with experimental core and surface temperature

4.4.5 EIS Results and Lithium Plating Discussion

EIS results and analysis of beginning of life and aged baseline/immersion cooled modules are shown in Figure 41. These plots clearly show a shift of mean resistance level, indicating ageing and SEI growth. Moreover, the valley and peak in the middle of the *ZTR* plots for the Fluid X immersion cooling case are shifted to the left compared to baseline and fresh cells. However, this shift seems to be very mild, indicating that even though Li plating occurs, it may not be the most dominant aging phenomenon.

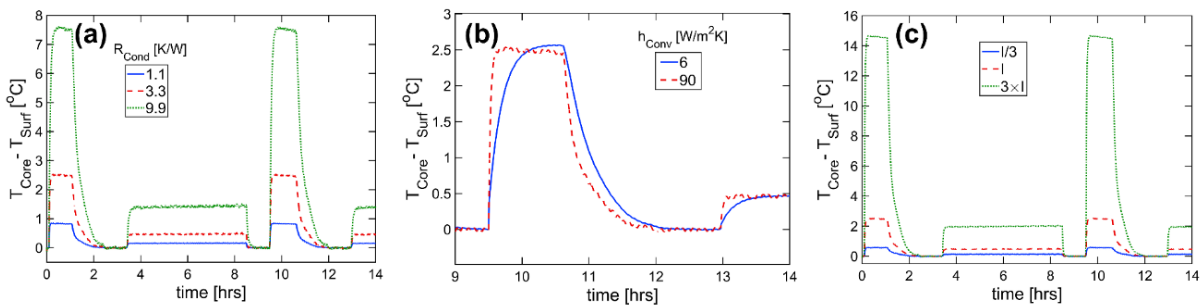

Figure 40. Sensitivity analysis for temperature difference between core and surface to (a) varying conductive resistance, (b) varying convective heat transfer coefficient, and (c) varying source current

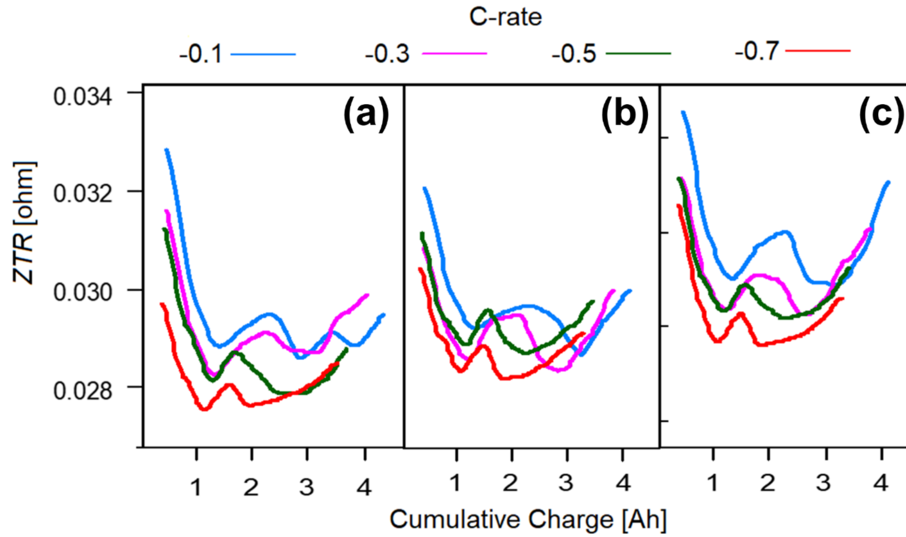

Figure 41. ZTR as a function of cumulative charge from Pseudo-EIS measurements for (a) Fresh cell, (b) cell aged in air for 60 cycles, (c) cell aged with Fluid X immersion cooling for 60 cycles [124].

4-5. Nomenclature

A	surface area (m^2)
C	specific heat ($Jkg^{-1}K^{-1}$)
f	frequency (Hz)
h	convective heat transfer coefficient ($Wm^{-2}K^{-1}$)
I	current (A)
m	mass of cell (kg)
Q	heat transfer (W)
R	thermal resistance (KW^{-1})
R_e	electrical resistance (Ω)
T	temperature (K)
t	time (s)
U	open circuit voltage (V)
V	voltage (V)
ZTR	impendence at transition frequency (Ω)
ε	emissivity
σ	Stefan-Boltzmann constant, ($5.67\times10^{-8}\ Wm^{-2}K^{-4}$)

Subscripts

Cell	cell
Cond	conduction
Conv	convection
Core	core of the cell
f	surrounding fluid
Gen	generation
OC	open circuit
P	constant pressure
Rad	radiation
Surf	surface
tr	transition

REFERENCES

[1] Azarfar, S., Movahedirad, S., Sarbanha, A. A., Norouzbeigi, R., and Beigzadeh, B., 2016, "Low Cost and New Design of Transient Hot-Wire Technique for the Thermal Conductivity Measurement of Fluids," Applied Thermal Engineering, **105**, pp. 142–150.

[2] Zhao, D., Qian, X., Gu, X., Jajja, S. A., and Yang, R., 2016, "Measurement Techniques for Thermal Conductivity and Interfacial Thermal Conductance of Bulk and Thin Film Materials," Journal of Electronic Packaging, **138**(4), p. 040802.

[3] Al-Ajlan, S. A., 2006, "Measurements of Thermal Properties of Insulation Materials by Using Transient Plane Source Technique," Applied Thermal Engineering, **26**(17–18), pp. 2184–2191.

[4] Nan, C. W., Birringer, R., Clarke, D. R., and Gleiter, H., 1997, "Effective Thermal Conductivity of Particulate Composites with Interfacial Thermal Resistance," Journal of Applied Physics, **81**(10), pp. 6692–6699.

[5] Xamán, J., Lira, L., and Arce, J., 2009, "Analysis of the Temperature Distribution in a Guarded Hot Plate Apparatus for Measuring Thermal Conductivity," Applied Thermal Engineering, **29**(4), pp. 617–623.

[6] Mathis, N., 2000, "Transient Thermal Conductivity Measurements: Comparison of Destructive and Nondestructive Techniques," High Temperatures - High Pressures, **32**(3), pp. 321–327.

[7] Parker, W. J., Jenkins, R. J., Butler, C. P., and Abbott, G. L., 1961, "Flash Method of Determining Thermal Diffusivity, Heat Capacity, and Thermal Conductivity," Journal of Applied Physics, **32**(9), pp. 1679–1684.

[8] Min, S., Blumm, J., and Lindemann, A., 2007, "A New Laser Flash System for Measurement of the Thermophysical Properties," Thermochimica Acta, **455**(1–2), pp. 46–49.

[9] Palacios, A., Cong, L., Navarro, M. E., Ding, Y., and Barreneche, C., 2019, "Thermal Conductivity Measurement Techniques for Characterizing Thermal Energy Storage Materials – A Review," Renewable and Sustainable Energy Reviews, **108**, pp. 32–52.

[10] Ostanek, J., Shah, K., and Jain, A., 2016, "Measurement Sensitivity Analysis of the Transient Hot Source Technique Applied to Flat and Cylindrical Samples," Journal of Thermal Science and Engineering Applications, **9**(1), p. 011002.

[11] Wang, H., and Sen, M., 2009, "Analysis of the 3-Omega Method for Thermal Conductivity Measurement," International Journal of Heat and Mass Transfer, **52**(7–8), pp. 2102–2109.

[12] Zhang, X., Fujiwara, S., and Fujii, M., 2000, "Measurements of Thermal Conductivity and Electrical Conductivity of a Single Carbon Fiber," International Journal of Thermophysics, **21**(4), pp. 965–980.

[13] Malen, J. A., Baheti, K., Tong, T., Zhao, Y., Hudgings, J. A., and Majumdar, A., 2011, "Optical Measurement of Thermal Conductivity Using Fiber Aligned Frequency Domain Thermoreflectance," Journal of Heat Transfer, **133**(8), p. 081601.

[14] Rusconi, R., Rodari, E., and Piazza, R., 2006, "Optical Measurements of the Thermal Properties of Nanofluids," Applied Physics Letters, **89**(26).

[15] Popov, Y. A., Pribnow, D. F. C., Sass, J. H., Williams, C. F., and Burkhardt, H., 1999, "Characterization of Rock Thermal Conductivity by High-Resolution Optical Scanning," Geothermics, **28**(2), pp. 253–276.

[16] Vishwakarma, V., and Jain, A., 2014, "Measurement of In-Plane Thermal Conductivity and Heat Capacity of Separator in Li-Ion Cells Using a Transient DC Heating Method," Journal of Power Sources, **272**, pp. 378–385.
[17] Cahill, D. G., 1990, "Thermal Conductivity Measurement from 30 to 750 K: The 3ω Method," Review of Scientific Instruments, **61**(2), pp. 802–808.
[18] Oh, D. W., Jain, A., Eaton, J. K., Goodson, K. E., and Lee, J. S., 2008, "Thermal Conductivity Measurement and Sedimentation Detection of Aluminum Oxide Nanofluids by Using the 3ω Method," International Journal of Heat and Fluid Flow, **29**(5), pp. 1456–1461.
[19] Cheaito, R., Sood, A., Yates, L., Bougher, T. L., Cheng, Z., Asheghi, M., Graham, S., and Goodson, K., 2017, "Thermal Conductivity Measurements on Suspended Diamond Membranes Using Picosecond and Femtosecond Time-Domain Thermoreflectance," Proceedings of the 16th InterSociety Conference on Thermal and Thermomechanical Phenomena in Electronic Systems, ITherm 2017, pp. 706–710.
[20] Burzo, M. G., Raad, P. E., Lee, T., and Komarov, P. L., 2012, "Thermal Conductivity Measurements of Novel SOI Films Using Submicron Thermography and Transient Thermoreflectance," Annual IEEE Semiconductor Thermal Measurement and Management Symposium, pp. 150–156.
[21] Wang, X., Shakouri, A., Mavrokefalos, A., Lee, Y., Kong, H., and Shi, L., 2010, "Thermoreflectance Imaging Measurement of In-Plane Thermal Properties of Thin-Film Structures," Annual IEEE Semiconductor Thermal Measurement and Management Symposium, pp. 235–239.
[22] Cahill, D. G., Goodson, K., and Majumdar, A., 2002, "Thermometry and Thermal Transport in Micro/Nanoscale Solid-State Devices and Structures," Journal of Heat Transfer, **124**(2), p. 223.
[23] Langenberg, E., Ferreiro-Vila, E., Leborán, V., Fumega, A. O., Pardo, V., and Rivadulla, F., 2016, "Analysis of the Temperature Dependence of the Thermal Conductivity of Insulating Single Crystal Oxides," APL Materials, **4**(10), p. 104815.
[24] Zheng, Q., Li, C., Rai, A., Leach, J. H., Broido, D. A., and Cahill, D. G., 2019, "Thermal Conductivity of GaN, <math> <mmultiscripts> <mi>GaN</Mi> <mprescripts/> <none/> <mn>71</Mn> </Mmultiscripts> </Math> , and SiC from 150 K to 850 K," Physical Review Materials, **3**(1), p. 014601.
[25] Ravoori, D., Alba, L., Prajapati, H., and Jain, A., 2018, "Investigation of Process-Structure-Property Relationships in Polymer Extrusion Based Additive Manufacturing through in Situ High Speed Imaging and Thermal Conductivity Measurements," Additive Manufacturing, **23**, pp. 132–139.
[26] Costa, S. F., Duarte, F. M., and Covas, J. A., 2017, "Estimation of Filament Temperature and Adhesion Development in Fused Deposition Techniques," Journal of Materials Processing Technology, **245**, pp. 167–179.
[27] Zhu, P., Lowke, J. J., and Morrow, R., 1992, "A Unified Theory of Free Burning Arcs, Cathode Sheaths and Cathodes," Journal of Physics D: Applied Physics, **25**(8), pp. 1221–1230.
[28] Raoelison, R. N., Fuentes, A., Pouvreau, C., Rogeon, P., Carré, P., and Dechalotte, F., 2014, "Modeling and Numerical Simulation of the Resistance Spot Welding of Zinc Coated Steel Sheets Using Rounded Tip Electrode: Analysis of Required Conditions," Applied Mathematical Modelling, **38**(9–10), pp. 2505–2521.

[29] Wu, D., Huang, C., Ma, Y., Wang, Y., Wang, F., and Guo, C., 2019, "Enhanced Thermal Conductivity of Welding Spots by Coatings Cupric Acetate on Copper Nanoparticle Solders," Materials Research Express, **6**(8), p. 085091.
[30] Öztürk, E., Aksöz, S., Keşlioğlu, K., and Maraşlı, N., 2013, "The Measurement of Thermal Conductivity Variation with Temperature for Sn-20wt.% In Based Lead-Free Ternary Solders," Thermochimica Acta, **554**, pp. 63–70.
[31] Bilek, J., Atkinson, J. K., and Wakeham, W. A., 2006, "Thermal Conductivity of Molten Lead-Free Solders," International Journal of Thermophysics, **27**(1), pp. 92–102.
[32] Hahn, J., Marconnet, A., and Reid, T., 2016, "Using Do-It-Yourself Practitioners as Lead Users: A Case Study on the Hair Care Industry," Journal of Mechanical Design, **138**(10), p. 101107.
[33] Incropera, F. P., DeWitt, D. P., Bergman, T. L., and Lavine, A. S., 2007, *Fundamentals of Heat and Mass Transfer*, John Wiley & Sons.
[34] Churchill, S. W., and Chu, H. H. S., 1975, "Correlating Equations for Laminar and Turbulent Free Convection from a Horizontal Cylinder," International Journal of Heat and Mass Transfer, **18**(9), pp. 1049–1053.
[35] Churchill, S. W., and Bernstein, M., 1977, "A Correlating Equation for Forced Convection From Gases and Liquids to a Circular Cylinder in Crossflow," Journal of Heat Transfer, **99**(2), p. 300.
[36] Anthony, D., Sarkar, D., and Jain, A., 2016, "Non-Invasive, Transient Determination of the Core Temperature of a Heat-Generating Solid Body," Scientific Reports, **6**(1), p. 35886.
[37] Anthony, D., Wong, D., Wetz, D., and Jain, A., 2017, "Non-Invasive Measurement of Internal Temperature of a Cylindrical Li-Ion Cell during High-Rate Discharge," International Journal of Heat and Mass Transfer, **111**, pp. 223–231.
[38] Croteau, C. B., and Krishnankutty, D., 2017, "Cyber-Physical Security Research at UMBC's Eclipse Lab," Mechanical Engineering, **139**(03), pp. S18–S23.
[39] Hu, N., Ye, M., and Wei, S., 2019, "Surviving Information Leakage Hardware Trojan Attacks Using Hardware Isolation," IEEE Transactions on Emerging Topics in Computing, **7**(2), pp. 253–261.
[40] Nguyen, L. N., Cheng, C.-L., Prvulovic, M., and Zajic, A., 2019, "Creating a Backscattering Side Channel to Enable Detection of Dormant Hardware Trojans," IEEE Transactions on Very Large Scale Integration (VLSI) Systems, **27**(7), pp. 1561–1574.
[41] Narasimhan, S., Du, D., Chakraborty, R. S., Paul, S., Wolff, F. G., Papachristou, C. A., Roy, K., and Bhunia, S., 2013, "Hardware Trojan Detection by Multiple-Parameter Side-Channel Analysis," IEEE Transactions on Computers, **62**(11), pp. 2183–2195.
[42] Hu, K., Nowroz, A. N., Reda, S., and Koushanfar, F., 2013, "High-Sensitivity Hardware Trojan Detection Using Multimodal Characterization," *2013 Design, Automation & Test in Europe Conference & Exhibition (DATE)*, IEEE, pp. 1271–1276.
[43] Tehranipoor, M., and Koushanfar, F., 2010, "A Survey of Hardware Trojan Taxonomy and Detection," IEEE Design & Test of Computers, **27**(1), pp. 10–25.
[44] Narasimhan, S., Wang, X., Du, D., Chakraborty, R. S., and Bhunia, S., 2011, "TeSR: A Robust Temporal Self-Referencing Approach for Hardware Trojan Detection," *2011 IEEE International Symposium on Hardware-Oriented Security and Trust*, IEEE, pp. 71–74.
[45] Wang, Q., Chen, D., and Geiger, R. L., 2018, "Transparent Side Channel Trigger Mechanism on Analog Circuits with PAAST Hardware Trojans," *2018 IEEE International Symposium on Circuits and Systems (ISCAS)*, IEEE, pp. 1–4.

[46] Amelian, A., and Borujeni, S. E., 2018, "A Side-Channel Analysis for Hardware Trojan Detection Based on Path Delay Measurement," Journal of Circuits, Systems and Computers, **27**(09), p. 1850138.
[47] Cha, B., and Gupta, S. K., 2013, "Trojan Detection via Delay Measurements: A New Approach to Select Paths and Vectors to Maximize Effectiveness and Minimize Cost," *Design, Automation & Test in Europe Conference & Exhibition, 2013*, IEEE Conference Publications, New Jersey, pp. 1265–1270.
[48] Bao, C., Forte, D., and Srivastava, A., 2015, "Temperature Tracking: Toward Robust Run-Time Detection of Hardware Trojans," IEEE Transactions on Computer-Aided Design of Integrated Circuits and Systems, **34**(10), pp. 1577–1585.
[49] Salmani, H., and Tehranipoor, M., 2012, "Layout-Aware Switching Activity Localization to Enhance Hardware Trojan Detection," IEEE Transactions on Information Forensics and Security, **7**(1 PART 1), pp. 76–87.
[50] Hou, B., He, C., Wang, L., En, Y., and Xie, S., 2014, "Hardware Trojan Detection via Current Measurement: A Method Immune to Process Variation Effects," *2014 10th International Conference on Reliability, Maintainability and Safety (ICRMS)*, IEEE, pp. 1039–1042.
[51] Xiao, K., Zhang, X., and Tehranipoor, M., 2013, "A Clock Sweeping Technique for Detecting Hardware Trojans Impacting Circuits Delay," IEEE Design and Test, **30**(2), pp. 26–34.
[52] Yier Jin, Maliuk, D., and Makris, Y., 2012, "Post-Deployment Trust Evaluation in Wireless Cryptographic ICs," *2012 Design, Automation & Test in Europe Conference & Exhibition*, W. Rosenstiel, and L. Thiele, eds., IEEE, pp. 965–970.
[53] Dubeuf, J., Hely, D., and Karri, R., 2013, "Run-Time Detection of Hardware Trojans: The Processor Protection Unit," *2013 18TH IEEE EUROPEAN TEST SYMPOSIUM (ETS)*, IEEE, pp. 1–6.
[54] Xuehui Zhang, and Tehranipoor, M., 2013, "RON: An on-Chip Ring Oscillator Network for Hardware Trojan Detection," *2011 Design, Automation & Test in Europe*, IEEE, pp. 1–6.
[55] Narasimhan, S., Yueh, W., Wang, X., Mukhopadhyay, S., and Bhunia, S., 2012, "Improving IC Security against Trojan Attacks through Integration of Security Monitors," IEEE Design and Test of Computers, **29**(5), pp. 37–46.
[56] Davoodi, A., Li, M., and Tehranipoor, M., 2013, "A Sensor-Assisted Self-Authentication Framework for Hardware Trojan Detection," IEEE Design and Test, **30**(5), pp. 74–82.
[57] Kim, L. W., and Villasenor, J. D., 2015, "Dynamic Function Verification for System on Chip Security Against Hardware-Based Attacks," IEEE Transactions on Reliability, **64**(4), pp. 1229–1242.
[58] Soll, O., Korak, T., Muehlberghuber, M., and Hutter, M., 2014, "EM-Based Detection of Hardware Trojans on FPGAs," *2014 IEEE International Symposium on Hardware-Oriented Security and Trust (HOST)*, IEEE, pp. 84–87.
[59] Cao, Y., Chang, C. H., and Chen, S., 2014, "A Cluster-Based Distributed Active Current Sensing Circuit for Hardware Trojan Detection," IEEE Transactions on Information Forensics and Security, **9**(12), pp. 2220–2231.
[60] Ngo, X.-T., Exurville, I., Bhasin, S., Danger, J.-L., Guilley, S., Najm, Z., Rigaud, J.-B., and Robisson, B., 2015, "Hardware Trojan Detection by Delay and Electromagnetic Measurements," *Design, Automation & Test in Europe Conference & Exhibition (DATE), 2015*, IEEE Conference Publications, New Jersey, pp. 782–787.

[61] He, C., Hou, B., Wang, L., En, Y., and Xie, S., 2014, "A Novel Hardware Trojan Detection Method Based on Side-Channel Analysis and PCA Algorithm," *2014 10th International Conference on Reliability, Maintainability and Safety (ICRMS)*, IEEE, pp. 1043–1046.
[62] Oh, S. K., Lundh, J. S., Shervin, S., Chatterjee, B., Lee, D. K., Choi, S., Kwak, J. S., and Ryou, J.-H., 2019, "Thermal Management and Characterization of High-Power Wide-Bandgap Semiconductor Electronic and Photonic Devices in Automotive Applications," Journal of Electronic Packaging, **141**(2).
[63] Pandey, P., Oxley, C., Hopper, R., Ali, Z., and Duffy, A., 2019, "Infra-Red Thermal Measurement on a Low-Power Infra-Red Emitter in CMOS Technology," IET Science, Measurement & Technology, **13**(1), pp. 25–28.
[64] Andonova, A., Angelov, G., and Chernev, P., 2014, "Diagnostics of Packaged ICs By Infrared Thermography," *Proceedings of the 2014 37th International Spring Seminar on Electronics Technology*, IEEE, pp. 261–266.
[65] Hamann, H. F., Weger, A., Lacey, J. A., Hu, Z., Bose, P., Cohen, E., and Wakil, J., 2007, "Hotspot-Limited Microprocessors: Direct Temperature and Power Distribution Measurements," IEEE Journal of Solid-State Circuits, **42**(1), pp. 56–64.
[66] Cheng, H. C., Huang, T. C., Hwang, P. W., and Chen, W. H., 2016, "Heat Dissipation Assessment of through Silicon via (TSV)-Based 3D IC Packaging for CMOS Image Sensing," Microelectronics Reliability, **59**, pp. 84–94.
[67] Nowroz, A. N., Hu, K., Koushanfar, F., and Reda, S., 2014, "Novel Techniques for High-Sensitivity Hardware Trojan Detection Using Thermal and Power Maps," IEEE Transactions on Computer-Aided Design of Integrated Circuits and Systems, **33**(12), pp. 1792–1805.
[68] Tang, Y., Li, S., Zhang, F., and Fang, L., 2018, "Thermal Maps Based HT Detection Using Spatial Projection Transformation," IET Information Security, **12**(4), pp. 356–361.
[69] Zhong, J., and Wang, J., 2018, "Thermal Images Based Hardware Trojan Detection through Differential Temperature Matrix," Optik (Stuttg), **158**, pp. 855–860.
[70] Choobineh, L., Jones, J., and Jain, A., 2017, "Experimental and Numerical Investigation of Interdie Thermal Resistance in Three-Dimensional Integrated Circuits," Journal of Electronic Packaging, **139**(2), pp. 1–6.
[71] Wang, Z., Bovik, A. C., Sheikh, H. R., and Simoncelli, E. P., 2004, "Image Quality Assessment: From Error Visibility to Structural Similarity," IEEE Transactions on Image Processing, **13**(4), pp. 600–612.
[72] Brunet, D., Vrscay, E. R., and Zhou Wang, 2012, "On the Mathematical Properties of the Structural Similarity Index," IEEE Transactions on Image Processing, **21**(4), pp. 1488–1499.
[73] Gao, Y., Rehman, A., and Wang, Z., 2011, "CW-SSIM Based Image Classification," *18th IEEE International Conference on Image Processing*, IEEE, pp. 1249–1252.
[74] Pan, B., Qian, K., Xie, H., and Asundi, A., 2009, "Two-Dimensional Digital Image Correlation for in-Plane Displacement and Strain Measurement: A Review," Measurement Science and Technology, **20**(6), p. 062001.
[75] Sadek, S., Iskander, M. G., and Liu, J., 2003, "Accuracy of Digital Image Correlation for Measuring Deformations in Transparent Media," Journal of Computing in Civil Engineering, **17**(2), pp. 88–96.
[76] Brunelli, R., and Mich, O., 2001, "Histograms Analysis for Image Retrieval," Pattern Recognition, **34**(8), pp. 1625–1637.

[77] Zhu, R., and Wang, Y., 2012, “Application of Improved Median Filter on Image Processing,” Journal of Computers, **7**(4), pp. 838–841.
[78] Shim, J., 2002, “Electrochemical Analysis for Cycle Performance and Capacity Fading of a Lithium-Ion Battery Cycled at Elevated Temperature,” Journal of Power Sources, **112**, pp. 222–230.
[79] Carter, R., and Love, C. T., 2018, “Modulation of Lithium Plating in Li-Ion Batteries with External Thermal Gradient,” ACS Applied Materials & Interfaces, **10**(31), pp. 26328–26334.
[80] Mishra, D., and Jain, A., 2021, “Multi-Mode Heat Transfer Simulations of the Onset and Propagation of Thermal Runaway in a Pack of Cylindrical Li-Ion Cells,” J Electrochem Soc, **168**(2), p. 020504.
[81] Xia, G., Cao, L., and Bi, G., 2017, “A Review on Battery Thermal Management in Electric Vehicle Application,” Journal of Power Sources, **367**, pp. 90–105.
[82] Mishra, D., and Jain, A., 2021, “Multi-Mode Heat Transfer Simulations of the Onset and Propagation of Thermal Runaway in a Pack of Cylindrical Li-Ion Cells,” Journal of The Electrochemical Society, **168**(2), p. 020504.
[83] Shah, K., Drake, S. J., Wetz, D. A., Ostanek, J. K., Miller, S. P., Heinzel, J. M., and Jain, A., 2014, “Modeling of Steady-State Convective Cooling of Cylindrical Li-Ion Cells,” Journal of Power Sources, **258**, pp. 374–381.
[84] Shah, K., Drake, S. J., Wetz, D. A., Ostanek, J. K., Miller, S. P., Heinzel, J. M., and Jain, A., 2014, “An Experimentally Validated Transient Thermal Model for Cylindrical Li-Ion Cells,” Journal of Power Sources, **271**, pp. 262–268.
[85] Chalise, Di., Shah, K., Prasher, R., and Jain, A., 2018, “Conjugate Heat Transfer Analysis of Thermal Management of a Li-Ion Battery Pack,” Journal of Electrochemical Energy Conversion and Storage, **15**(1), pp. 1–8.
[86] Dan, D., Yao, C., Zhang, Y., Zhang, H., Zeng, Z., and Xu, X., 2019, “Dynamic Thermal Behavior of Micro Heat Pipe Array-Air Cooling Battery Thermal Management System Based on Thermal Network Model,” Applied Thermal Engineering, **162**, p. 114183.
[87] Zhang, H., Li, C., Zhang, R., Lin, Y., and Fang, H., 2020, “Thermal Analysis of a 6s4p Lithium-Ion Battery Pack Cooled by Cold Plates Based on a Multi-Domain Modeling Framework,” Applied Thermal Engineering, **173**, p. 115216.
[88] Behi, H., Karimi, D., Behi, M., Ghanbarpour, M., Jaguemont, J., Sokkeh, M. A., Gandoman, F. H., Berecibar, M., and van Mierlo, J., 2020, “A New Concept of Thermal Management System in Li-Ion Battery Using Air Cooling and Heat Pipe for Electric Vehicles,” Applied Thermal Engineering, **174**, p. 115280.
[89] Anthony, D., Wong, D., Wetz, D., and Jain, A., 2017, “Non-Invasive Measurement of Internal Temperature of a Cylindrical Li-Ion Cell during High-Rate Discharge,” International Journal of Heat and Mass Transfer, **111**, pp. 223–231.
[90] Anthony, D., Wong, D., Wetz, D., and Jain, A., 2017, “Improved Thermal Performance of a Li-Ion Cell through Heat Pipe Insertion,” Journal of The Electrochemical Society, **164**(6), pp. A961–A967.
[91] Shah, K., and Jain, A., 2015, “Modeling of Steady-State and Transient Thermal Performance of a Li-Ion Cell with an Axial Fluidic Channel for Cooling,” International Journal of Energy Research, **39**(4), pp. 573–584.
[92] Shah, K., McKee, C., Chalise, D., and Jain, A., 2016, “Experimental and Numerical Investigation of Core Cooling of Li-Ion Cells Using Heat Pipes,” Energy, **113**, pp. 852–860.

[93] Xie, Y., Zheng, J., Li, W., Lee, K., Zhang, Y., Liu, J., Dan, D., Wu, C., and Wang, P., 2020, "An Improved Electrothermal-coupled Model for the Temperature Estimation of an Air-cooled Battery Pack," International Journal of Energy Research, **44**(3), pp. 2037–2060.

[94] Amiribavandpour, P., Shen, W., and Kapoor, A., 2013, "Development of Thermal-Electrochemical Model for Lithium Ion 18650 Battery Packs in Electric Vehicles," *2013 IEEE Vehicle Power and Propulsion Conference (VPPC)*, IEEE, pp. 1–5.

[95] Smith, K., and Wang, C.-Y., 2006, "Power and Thermal Characterization of a Lithium-Ion Battery Pack for Hybrid-Electric Vehicles," Journal of Power Sources, **160**(1), pp. 662–673.

[96] Lin, X., Perez, H. E., Mohan, S., Siegel, J. B., Stefanopoulou, A. G., Ding, Y., and Castanier, M. P., 2014, "A Lumped-Parameter Electro-Thermal Model for Cylindrical Batteries," Journal of Power Sources, **257**, pp. 1–11.

[97] Damay, N., Forgez, C., Bichat, M.-P., and Friedrich, G., 2015, "Thermal Modeling of Large Prismatic LiFePO 4 /Graphite Battery. Coupled Thermal and Heat Generation Models for Characterization and Simulation," Journal of Power Sources, **283**, pp. 37–45.

[98] LeBel, F.-A., Wilke, S., Schweitzer, B., Roux, M.-A., Al-Hallaj, S., and Trovao, J. P. F., 2016, "A Lithium-Ion Battery Electro-Thermal Model of Parallellized Cells," *2016 IEEE 84th Vehicular Technology Conference (VTC-Fall)*, IEEE, pp. 1–6.

[99] Liu, F., Lan, F., and Chen, J., 2016, "Dynamic Thermal Characteristics of Heat Pipe via Segmented Thermal Resistance Model for Electric Vehicle Battery Cooling," Journal of Power Sources, **321**, pp. 57–70.

[100] Ramotar, L., Rohrauer, G. L., Filion, R., and MacDonald, K., 2017, "Experimental Verification of a Thermal Equivalent Circuit Dynamic Model on an Extended Range Electric Vehicle Battery Pack," Journal of Power Sources, **343**, pp. 383–394.

[101] Jiang, Z. Y., Qu, Z. G., Zhang, J. F., and Rao, Z. H., 2020, "Rapid Prediction Method for Thermal Runaway Propagation in Battery Pack Based on Lumped Thermal Resistance Network and Electric Circuit Analogy," Applied Energy, **268**.

[102] Cui, X., Zeng, J., Zhang, H., Yang, J., Qiao, J., Li, J., and Li, W., 2020, "Optimization of the Lumped Parameter Thermal Model for Hard-Cased Li-Ion Batteries," Journal of Energy Storage, **32**.

[103] Ganesan, V. v., and Jain, A., 2021, "Computationally-Efficient Thermal Simulations of Large Li-Ion Battery Packs Using Submodeling Technique," International Journal of Heat and Mass Transfer, **165**, p. 120616.

[104] Mohammadian, S. K., and Zhang, Y., 2015, "Thermal Management Optimization of an Air-Cooled Li-Ion Battery Module Using Pin-Fin Heat Sinks for Hybrid Electric Vehicles," Journal of Power Sources, **273**, pp. 431–439.

[105] Lu, Z., Meng, X. Z., Wei, L. C., Hu, W. Y., Zhang, L. Y., and Jin, L. W., 2016, "Thermal Management of Densely-Packed EV Battery with Forced Air Cooling Strategies," Energy Procedia, **88**, pp. 682–688.

[106] Akbarzadeh, M., Jaguemont, J., Kalogiannis, T., Karimi, D., He, J., Jin, L., Xie, P., van Mierlo, J., and Berecibar, M., 2021, "A Novel Liquid Cooling Plate Concept for Thermal Management of Lithium-Ion Batteries in Electric Vehicles," Energy Conversion and Management, **231**, p. 113862.

[107] Chung, Y., and Kim, M. S., 2019, "Thermal Analysis and Pack Level Design of Battery Thermal Management System with Liquid Cooling for Electric Vehicles," Energy Conversion and Management, **196**, pp. 105–116.

[108] Anthony, D., Wong, D., Wetz, D., and Jain, A., 2017, "Improved Thermal Performance of a Li-Ion Cell through Heat Pipe Insertion," Journal of The Electrochemical Society, **164**(6), pp. A961–A967.
[109] Smith, J., Singh, R., Hinterberger, M., and Mochizuki, M., 2018, "Battery Thermal Management System for Electric Vehicle Using Heat Pipes," International Journal of Thermal Sciences, **134**, pp. 517–529.
[110] Mostafavi, A., and Jain, A., 2021, "Dual-purpose Thermal Management of Li-ion Cells Using Solid-state Thermoelectric Elements," International Journal of Energy Research, **45**(3), pp. 4303–4313.
[111] Alaoui, C., 2013, "Solid-State Thermal Management for Lithium-Ion EV Batteries," IEEE Transactions on Vehicular Technology, **62**(1), pp. 98–107.
[112] Lu, M., Zhang, X., Ji, J., Xu, X., and Zhang, Y., 2020, "Research Progress on Power Battery Cooling Technology for Electric Vehicles," Journal of Energy Storage, **27**, p. 101155.
[113] Javani, N., Dincer, I., Naterer, G. F., and Yilbas, B. S., 2014, "Heat Transfer and Thermal Management with PCMs in a Li-Ion Battery Cell for Electric Vehicles," International Journal of Heat and Mass Transfer, **72**, pp. 690–703.
[114] Yuan, X., Tang, A., Shan, C., Liu, Z., and Li, J., 2020, "Experimental Investigation on Thermal Performance of a Battery Liquid Cooling Structure Coupled with Heat Pipe," Journal of Energy Storage, **32**, p. 101984.
[115] Bernagozzi, M., Georgoulas, A., Miché, N., Rouaud, C., and Marengo, M., 2021, "Novel Battery Thermal Management System for Electric Vehicles with a Loop Heat Pipe and Graphite Sheet Inserts," Applied Thermal Engineering, **194**, p. 117061.
[116] He, W., Zhang, G., Zhang, X., Ji, J., Li, G., and Zhao, X., 2015, "Recent Development and Application of Thermoelectric Generator and Cooler," Applied Energy, **143**, pp. 1–25.
[117] Wu, S., Lao, L., Wu, L., Liu, L., Lin, C., and Zhang, Q., 2022, "Effect Analysis on Integration Efficiency and Safety Performance of a Battery Thermal Management System Based on Direct Contact Liquid Cooling," Applied Thermal Engineering, **201**, p. 117788.
[118] Suresh Patil, M., Seo, J.-H., and Lee, M.-Y., 2021, "A Novel Dielectric Fluid Immersion Cooling Technology for Li-Ion Battery Thermal Management," Energy Conversion and Management, **229**, p. 113715.
[119] Wang, Y., Rao, Z., Liu, S., Li, X., Li, H., and Xiong, R., 2021, "Evaluating the Performance of Liquid Immersing Preheating System for Lithium-Ion Battery Pack," Applied Thermal Engineering, **190**, p. 116811.
[120] Tan, X., Lyu, P., Fan, Y., Rao, J., and Ouyang, K., 2021, "Numerical Investigation of the Direct Liquid Cooling of a Fast-Charging Lithium-Ion Battery Pack in Hydrofluoroether," Applied Thermal Engineering, **196**, p. 117279.
[121] Anthony, D., Wong, D., Wetz, D., and Jain, A., 2017, "Non-Invasive Measurement of Internal Temperature of a Cylindrical Li-Ion Cell during High-Rate Discharge," International Journal of Heat and Mass Transfer, **111**, pp. 223–231.
[122] Drake, S. J., Martin, M., Wetz, D. A., Ostanek, J. K., Miller, S. P., Heinzel, J. M., and Jain, A., 2015, "Heat Generation Rate Measurement in a Li-Ion Cell at Large C-Rates through Temperature and Heat Flux Measurements," Journal of Power Sources, **285**, pp. 266–273.
[123] "3M^{TM} Novec^{TM} 7000 Engineered Fluid | 3M United States" [Online]. Available: https://www.3m.com/3M/en_US/p/d/b5005006004/. [Accessed: 05-Apr-2022].
[124] Gaberšček, M., 2021, "Understanding Li-Based Battery Materials via Electrochemical Impedance Spectroscopy," Nature Communications, **12**(1), p. 6513.

[125] Koleti, U. R., Dinh, T. Q., and Marco, J., 2020, "A New On-Line Method for Lithium Plating Detection in Lithium-Ion Batteries," Journal of Power Sources, **451**, p. 227798.
[126] Hales, A., Marzook, M. W., Bravo Diaz, L., Patel, Y., and Offer, G., 2020, "The Surface Cell Cooling Coefficient: A Standard to Define Heat Rejection from Lithium Ion Battery Pouch Cells," Journal of The Electrochemical Society, **167**(2), p. 020524.
[127] Parhizi, M., Ahmed, M. B., and Jain, A., 2017, "Determination of the Core Temperature of a Li-Ion Cell during Thermal Runaway," Journal of Power Sources, **370**, pp. 27–35.
[128] Forgez, C., Vinh Do, D., Friedrich, G., Morcrette, M., and Delacourt, C., 2010, "Thermal Modeling of a Cylindrical LiFePO4/Graphite Lithium-Ion Battery," Journal of Power Sources, **195**(9), pp. 2961–2968.
[129] Hatchard, T. D., MacNeil, D. D., Stevens, D. A., Christensen, L., & Dahn, J. R., 2000, "Importance of Heat Transfer by Radiation in Li-Ion Batteries during Thermal Abuse," Electrochemical and Solid-State Letters, **3**(7), p. 305.
[130] Troxler, Y., Wu, B., Marinescu, M., Yufit, V., Patel, Y., Marquis, A. J., Brandon, N. P., and Offer, G. J., 2014, "The Effect of Thermal Gradients on the Performance of Lithium-Ion Batteries," Journal of Power Sources, **247**, pp. 1018–1025.
[131] Zhao, Y., Patel, Y., Zhang, T., and Offer, G. J., 2018, "Modeling the Effects of Thermal Gradients Induced by Tab and Surface Cooling on Lithium Ion Cell Performance," Journal of The Electrochemical Society, **165**(13), pp. A3169–A3178.
[132] Incropera, F. P., DeWitt, D. P., Bergman, T. L., and Lavine, A. S., 1996, *Fundamentals of Heat and Mass Transfer*, Wiley New York.
[133] Churchill, S. W., and Chu, H. H. S., 1975, "Correlating Equations for Laminar and Turbulent Free Convection from a Horizontal Cylinder," International Journal of Heat and Mass Transfer, **18**(9), pp. 1049–1053.
[134] Churchill, S. W., and Bernstein, M., 1977, "A Correlating Equation for Forced Convection From Gases and Liquids to a Circular Cylinder in Crossflow," Journal of Heat Transfer, **99**(2), pp. 300–306.

Chapter 5

Conclusion

5-1. Conclusion

Chapter 2 directly addresses an important thermal metrology need for thermal characterization of thin wires that are used in a variety of engineering applications. The size of such wires often makes them unsuitable for both macroscale and microscale thermal conductivity measurement techniques. Using the well-known fin effect, this work develops a novel technique for determining thermal conductivity of a thin wire through a comparative measurement with a standard wire. Due to the small value of the radial Biot number, this method directly measures the axial thermal conductivity of the wire. Further, note that the method relies on a constant heat transfer coefficient around the wire, which is a reasonable assumption for the small temperature rise in the present experiments, but may break down due to non-linear radiative heat transfer at larger temperature differences. Results are shown to be in good agreement with independent measurements. The technique discussed here offers key advantages over traditional techniques such as laser flash and transient plane source methods, which are not applicable for direct measurements on wires. Further, the method is non-invasive and is unaffected by thermal contact resistances since temperature measurement is carried out using an infrared camera. The method may be applicable for several applications where thermal performance of wires is important to understand and optimize.

Chapter 3 presents measurement of temperature field of the transistor plane of a two-die 3D IC thermal test chip through backside infrared imaging to detect unusual activities simulated to induce the behavior of hardware trojans. Chips that are fabricated and assembled globally,

including by external manufacturers are inherently prone to the insertion of malicious hardware. Detection of such hardware Trojans is an ongoing security concern. This work contributes towards this important technological need by examining the use of temperature signals to detect Trojans specifically for a 3D IC. Similar to any detection process, the time to detect and occurrence of false positives/negatives are important considerations, which are addressed in this project. Four candidate image processing algorithms are compared, and strategies for improved performance are identified. The proposed techniques can detect the hardware Trojan effectively and can possibly be improved even further by a synergistic combination of multiple methods. Results presented in this work may help ensure the security of present and future semiconductor chips from hardware Trojans.

Chapter 4 presents the analysis carried out to study the accelerated aging for specified lithium-ion cells. Despite the promising nature of immersion cooling for Li-ion battery packs, several open questions remain, especially about the impact of immersion cooling on ageing of cells. The present work contributes towards addressing one of these through experimental and theoretical investigation of capacity fade caused by immersion cooling. Through a hypothesis-driven comparison of experimental measurements and theoretical modeling, a comprehensive understanding of this interesting and important phenomenon is developed. All the expected hypotheses in this study, targeting accelerated aging of cells, are examined one by one, viz., absence of radiative heat dissipation, non-uniform temperature distribution in radial direction and lithium plating. Experimental data, analytical models as well as non-intrusive electrochemical measurements are utilized to complete the study. The theoretical model for surface temperature measurements matches fairly well with the experimental measurements carried out, in both, baseline as well as Fluid X cases. From the findings of core and surface temperature model, it can be observed that for the baseline as well as Fluid X case with thermocouples inserted at the core

of the cell gives experimental measurements matching with the discussed coupled equation model. It can be concluded that these theoretical models are accurate enough to predict the core as well as surface temperatures of the cells under immersed cooling. EIS results approve the ageing and SEI growth; however, it cannot be denied that that the lithium plating might be marginally responsible for the accelerated ageing. It is expected that the analysis in this work may contribute towards further development and eventual implementation of immersion cooling for Li-ion battery packs in a manner that provides effective thermal management with minimal potential risks to electrochemical performance.

BIOGRAPHICAL INFORMATION

Swapnil Suryakant Salvi received his Bachelor of Engineering degree in Mechanical Engineering from University of Mumbai, India. Before coming to the USA, he completed his Master of Technology in Mechanical Engineering in June 2018 from the Indian Institute of Technology at Ropar, India. He started his Ph.D. in Mechanical Engineering at the University of Texas at Arlington in Fall 2018. His research area includes heat transfer, infrared thermography and thermal property characterization of Li-ion batteries and other engineering systems. He worked as an Intern at Southwest Research Institute (SwRI), San Antonio TX in Summer 2021. Soon, he aspires to pursue his career in industry as Research and Development Engineer.

Email: swapnilsalvi1993@gmail.com